Verifying the suitability of uncoupled numerical methods for solving vehicle-bridge interaction problems

Arturo González, Enrique Covián & Miguel Casero

Published online: 09 Feb 2022.

Submit your article to this journal ⏍

Article views: 826

View related articles ⏍

View Crossmark data ⏍

Taylor & Francis
Taylor & Francis Group

Verifying the suitability of uncoupled numerical methods for solving vehicle-bridge interaction problems

Arturo González[a] (ID), Enrique Covián[b] (ID) and Miguel Casero[a] (ID)

[a]School of Civil Engineering, University College Dublin, Dublin, Ireland; [b]Polytechnic School of Mieres, University of Oviedo, Mieres, Spain

ABSTRACT

The response of a structure subjected to a moving load can be obtained using coupled or uncoupled methods. The uncoupled method is often preferred since modal superposition is applicable, which implies computational efficiency and ease of implementation. However, the uncoupled method ignores the changes in the dynamic features of the combined structural system due to the time-varying location of the load. This paper analyses the extent to which the accuracy of the uncoupled method is affected by these changes. First, a parametric study is conducted on two discretized beam models traversed by a sprung mass at a constant speed. The error associated with the uncoupled method is calculated using the coupled solution as a reference. The influence of the load to structure mass and frequency ratios and the speed of the vehicle on the error is quantified. Heavier loads travelling at higher speeds are found to increase the inaccuracy of the uncoupled method. Then, the analysis is extended to a half-car travelling on a rough profile. Although errors from the uncoupled simulation remain low for the range of parameters under investigation, they may not be acceptable in some applications, i.e., the training of an algorithm for early damage detection.

1. Introduction

The response of a structure is often impacted by effects arising from the interaction with its surrounding environment. The research on this field falls within coupled mechanics, covering interactions with the soil, the foundation, a fluid, the wind, or other structures such as moving loads. This paper investigates the latter, where typical applications include the assessment of a bridge traversed by a vehicle or a crane subjected to a moving trolley (Milana, Banisoleiman, & González, 2021). The moving load problem, labelled as vehicle-bridge interaction (VBI) in the context of this paper, has an extensive literature built upon numerical methods that solve the equations of motion governing the structural response. Some reference sources giving background information and a general overview of numerical issues around the moving load problem include (Frýba, 1999; González, 2010; Michaltsos & Raftoyiannis, 2012; Yang, Yao, & Wu, 2004; Yu & Chan, 2007; Zhai, Han, Chen, Ling, & Zhu, 2019; Zhai et al., 2013).

Essentially, the available numerical methods can be grouped into two main approaches: uncoupled and coupled. The former is generally preferred over the latter due to its ease of implementation, computational efficiency (i.e., modal superposition applies), and robustness against numerical instability, although the need for an iterative procedure may be perceived as a drawback. Nevertheless, there is an underlying error in the uncoupled approach incurred by omitting the coupled nature of the problem. The magnitude of this

error is rarely reported in the literature, and therefore it is necessary to quantify it.

Some applications, such as moving force identification theory (Chan, Yu, Law, & Yung, 2001; Gonzalez, Rowley, & OBrien, 2008; Rowley, OBrien, Gonzalez, & Znidaric, 2009) are strictly based on an uncoupled approach, where the global mass, stiffness, and damping matrices of a finite element model (FEM) of the structure are assumed to be time-invariant. In other applications like the estimation of the dynamic amplification factor (DAF) (Cantero, González, & Obrien, 2009; Deng, Yu, Zou, & Cai, 2015; Gonzalez, Rattigan, OBrien, & Caprani, 2008; OBrien, Rattigan, Gonzalez, Dowling, & Znidaric, 2009) or the development of structural health monitoring techniques (Zhu & Law, 2015), uncoupled (Cantero, Gonzalez, & OBrien, 2011; Mohammed & González, 2017; Zhu & Law, 2002) and coupled approaches can be found indistinctively.

The uncoupled approach assumes that the effect of the time-varying properties of the VBI system on the dynamic features of the response is negligible compared to considering the bridge on its own, i.e., the frequencies and mode shapes in forced and free vibration are approximately equal. This paper aims to address whether the uncoupled assumption is reasonable or not. Past research agrees on three parameters accounting for the largest impact on the change in forced frequency:

- vehicle location (x_v) with respect to the span length (L) of the underlying structure,

- ratio of the vehicle mass (m_v) to the bridge mass (m_b), or mass ratio MR, and
- ratio of the frequency of the vehicle (f_v) to the first frequency of the bridge ($f_{b,1}$) in free vibration, or frequency ratio FR.

The Divine report (OECD, 1998) finds that significant system coupling occurs in medium and long-span bridges for MR as small as 0.05, i.e., $m_b = 20\, m_v$. On the other hand, the report suggests that no true VBI occurs for short-span bridges, i.e., $L < 10$ m. J. Z. Li, Su, and Fan (2003) report a maximum frequency variation of −14.6% for the 2nd natural frequency ($f_{b,2}$) in a numerical model of a 16 m span railway bridge. Based on numerical models of a simply supported beam traversed by a sprung mass, variations in $f_{b,1}$ of 46% are obtained for $L = 25$ m, $MR = 0.75$ and $FR = 0.75$ (Cantero & O'Brien, 2013) and up to 60% for $L = 30$ m, $MR = 0.5$ and FR close to 1 (Yang, Cheng, & Chang, 2013). Recent research relies on the pattern of the changes in forced frequency to identify damage (Feng, González, & Casero, 2021; González, Casero, & Feng, 2020). These changes appear to lose significance for x_v closer to the supports, low MR, and FR far apart from one.

The aforementioned theoretical changes in forced frequencies have been supported through field (Cantero, Ulker-Kaustell, & Karoumi, 2016; Matsuoka, Kaito, & Sogabe, 2020) and lab tests (Cantero, McGetrick, Kim, & OBrien, 2019). Kim, Jung, Kim, Kwon, and Feng (2003) report variations in the forced frequency of a bridge ($L = 46$ m) adding up to −5.4% between heavy and light vehicles where the former represents a MR of about 0.04 and the masses of the latter are negligible ($MR \approx 0$). Chang, Kim, and Borjigin (2014) identify frequency variations of −2.56% in the field ($MR = 0.04$, $FR = 1.83$), as well as −10.4% ($MR = 0.08$, $FR = 1.21$) and −9% ($MR = 0.08$, $FR = 1.46$) in lab experiments. Cantero, Hester, and Brownjohn (2017) successfully detect a trend in the measured frequencies and mode shapes of a steel bridge ($L = 36$ m) when a vehicle stops at several locations.

Although existing research has thrown some light into the topic of this paper, i.e., mainly relating changes in forced frequency, the influence of x_v, MR, and FR on the accuracy of the structural responses obtained by uncoupled VBI methods remains unanswered. The goal of this paper is to assess how the time-varying nature of the dynamic features in VBI models affects the accuracy of uncoupled methods. For this purpose, the values of the bending moment are obtained at the midspan section of a FEM of a simply supported beam using uncoupled and coupled methods. The vehicle is initially modelled as a sprung mass moving at a constant speed over the bridge. For this scenario, the response is obtained for two simply supported beams with span lengths $L = 15$ and 25 m, and properties based on a typical concrete bridge of the same span. The analysis is later extended to a half-car moving over the 15 m bridge. The use of a more complex vehicle implies that the number of parameters increases and the definition of the vehicle to bridge ratios is no longer straightforward. Montecarlo simulations are used to overcome this complication. Furthermore, the impact of a road profile is evaluated for a selected number of scenarios.

Section 2 presents the differences between VBI transient numerical formulations using uncoupled and coupled approaches. Section 3 applies eigenvalue analysis to quantify the variation in the dynamic features of the beam, such as frequencies and mode shapes, caused by changes in the properties of the sprung mass and its location. Section 4 establishes the error derived from using the uncoupled method for modelling the response of short and medium-span bridges as a function of the properties of the moving sprung mass and its speed. The accuracy of the uncoupled method is assessed by comparison to the solution given by the coupled method using the root mean square error (RMSE), and the relative error in the estimation of the maximum bending moment. Moreover, the contributions of MR, FR, and speed to the errors are quantified through the Sobol indices (Sobol, 2001). Section 5 deals with the evaluation of the accuracy of the uncoupled method when a half-car is travelling at a constant speed over a typical short span bridge allowing for a road profile in the simulation. Finally, Section 6 discusses the results presented in previous sections and Section 7 draws conclusions.

2. VBI simulation using coupled and uncoupled approaches

FEMs are best suited to reproduce the geometry of the vehicle and the bridge as well as to incorporate sophisticated elements and properties needed to mimic the structural response. In a preliminary stage, the stiffness, damping, and mass matrices of the vehicle and the bridge structural subsystems have to be defined for these FEMs, i.e., based on the equilibrium of forces and moments at each degree of freedom (DoF). The complexity of FEMs can vary significantly, ranging from planar (2 D) models where the vehicle is represented by a series of interconnected sprung masses and the response of the bridge is governed by its longitudinal modes of vibration, to 3 D models where the multi-body dynamics of the vehicle model allows for rolling and twisting, and transverse modes of vibration of the bridge are also taken into account.

In this paper, coupled and uncoupled approaches are implemented using a planar FEM of the bridge and, initially, a moving sprung mass, to facilitate a good visualization and understanding of the effect caused by the relevant parameters. After the parametric analysis is conducted, further simulations are carried out using a half-car. The bridge is modelled as a simply supported beam with a span length L (Figure 1), discretised into several Euler-Bernoulli beam elements (L_e = elementary length). There are 2 local DoFs at each end node of a beam element, namely the vertical displacement (u_i) and the in-plane rotation (θ_i). The sprung mass vehicle model is a 1-DoF model composed of a mass (m_v) connected to the bridge via a spring of stiffness k_v (centre of Figure 1). Therefore, the dynamic behaviour of the vehicle is characterised by a single frequency (f_v).

Figure 1 also represents the half-car vehicle model (left-hand side) consisting of two axle masses (m_1, m_2) connected
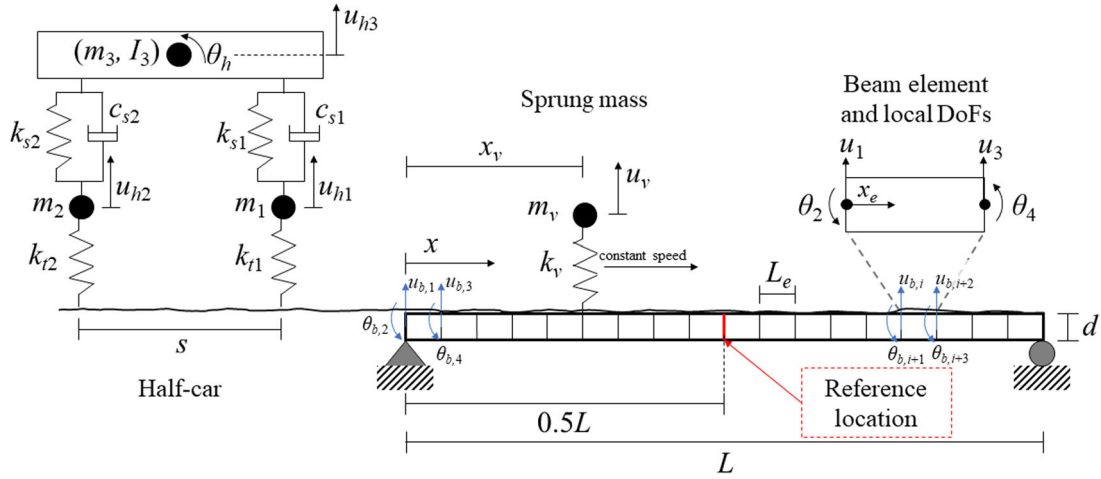
Figure 1. Vehicle and bridge models.

to the bridge and to another mass representing the body of the vehicle (m_3) through a series of springs and dashpots. The suspension system of the half-car is composed of springs (k_{s1}, k_{s2}) and dampers (c_{s1}, c_{s2}), whereas the tires are simply represented by springs (k_{t1}, k_{t2}). For all half-car parameters, sub-indices 1 and 2 correspond to the 1st and 2nd axle, respectively. The spacing between axles (s) is an additional parameter that is not contemplated in the simpler sprung mass model. The body mass is placed at the same distance from both axles and assigned a mass moment of inertia (I_3). The 4 DoFs of the half-car model represent the vertical displacement of the three vehicular masses (u_{h1}, u_{h2}, u_{h3}) and the rotation of the body mass (θ_h). Accordingly, the dynamic behaviour of the half-car model is governed by 4 frequencies representing the hop of the axles, plus the bounce and pitch of the body. All vehicle models are assumed to move at a constant speed over the bridge and to remain in permanent contact with the surface.

Once the stiffness, mass and damping matrices of the bridge and vehicle sub-systems have been defined, the engineer must decide whether to use an uncoupled or a coupled approach before establishing the differential equations of motion. Then, the equations are solved by implicit integration methods such as Hilbert-Hughes-Taylor, Wilson-θ or Newmark-β (Tedesco, McDougal, & Ross, 1999) to obtain displacements, velocities and accelerations for each DoF at each time step. Implicit methods ensure numerical stability and reduce numerical damping compared to explicit methods. In particular, the Wilson-θ method is an extension of the linear acceleration method that assumes a linear variation of the acceleration in the range [t, $t + \theta \Delta t$], where t represents a given moment in time, Δt is the time step and θ is a parameter of the method controlled by the user. Wilson-θ is the method applied in this paper with $\theta = 1.42$ to ensure unconditional stability (Weaver & Johnston, 1987).

2.1. The coupled approach

Equations (1) and (2) represent the equations of motion of the bridge and the vehicle, respectively:

$$[M_b] \cdot \{\ddot{u}_b\} + [C_b] \cdot \{\dot{u}_b\} + [K_b] \cdot \{u_b\} = \{F_b\} \qquad (1)$$

$$[M_v] \cdot \{\ddot{u}_v\} + [C_v] \cdot \{\dot{u}_v\} + [K_v] \cdot \{u_v\} = \{F_v\} \qquad (2)$$

where $[M_j]$, $[C_j]$ and $[K_j]$ are the mass, damping and stiffness matrices respectively; $\{F_j\}$ are the time-variant forces, and $\{\ddot{u}_j\}$, $\{\dot{u}_j\}$ and $\{u_j\}$ are the accelerations, velocities, and displacements respectively; for which sub-index $j = b$ refers to the bridge and sub-index $j = v$ refers to the vehicle. Damping is neglected here since its value is typically small in bridges. The bridge matrices have dimensions ($n \cdot n$), where n represents the total number of DoFs of the bridge. For the planar FEM under investigation, $n = (N_b + 1) \cdot 2$, where N_b is the number of elements in the bridge model.

For a moving load modelled as a single undamped sprung mass, Equation (2) can be simplified into the scalar Equation (3) related to a single DoF:

$$m_v \cdot \ddot{u}_v + k_v \cdot u_v = k_v \cdot (u_b + r)|_{x=x_v} \qquad (3)$$

where the term in the right-hand side of the equation represents the time-variant force F_v, which is the product of the vehicle spring stiffness by the relative displacement of the bridge at the location of the vehicle (x_v) plus the height of the irregularities of the bridge surface, i.e., a road or rail profile (r), at that same location. Thus, the force acting on the vehicle will vary as the sprung mass moves along the bridge.

As for the half-car model, the vehicle mass, damping, and stiffness matrices are given by Equations (4) (5) and (6), respectively:

$$[M_v] = \begin{bmatrix} m_3 & 0 & 0 & 0 \\ 0 & I_3 & 0 & 0 \\ 0 & 0 & m_1 & 0 \\ 0 & 0 & 0 & m_2 \end{bmatrix} \qquad (4)$$

$$[C_v] = \begin{bmatrix} c_{s1} + c_{s2} & (c_{s1} - c_{s2}) \cdot \frac{s}{2} & -c_{s1} & -c_{s2} \\ (c_{s1} - c_{s2}) \cdot \frac{s}{2} & (c_{s1} + c_{s2}) \cdot \left(\frac{s}{2}\right)^2 & -c_{s1} \cdot \frac{s}{2} & c_{s2} \cdot \frac{s}{2} \\ -c_{s1} & -c_{s1} \cdot \frac{s}{2} & c_{s1} & 0 \\ -c_{s2} & c_{s2} \cdot \frac{s}{2} & 0 & c_{s2} \end{bmatrix}$$

$$(5)$$

$$[K_v] = \begin{bmatrix} k_{s1} + k_{s2} & (k_{s1} - k_{s2}) \cdot \dfrac{s}{2} & -k_{s1} & -k_{s2} \\ (k_{s1} - k_{s2}) \cdot \dfrac{s}{2} & (k_{s1} + k_{s2}) \cdot \left(\dfrac{s}{2}\right)^2 & -k_{s1} \cdot \dfrac{s}{2} & k_{s2} \cdot \dfrac{s}{2} \\ -k_{s1} & -k_{s1} \cdot \dfrac{s}{2} & k_{s1} + k_{t1} & 0 \\ -k_{s2} & k_{s2} \cdot \dfrac{s}{2} & 0 & k_{s2} + k_{t2} \end{bmatrix} \tag{6}$$

where the parameters of the vehicle have been defined in Figure 1 and the 1st, 2nd, 3rd, and 4th rows/columns of the matrices correspond to the vertical displacement of the body mass (u_{h3}), in-plane rotation of the body mass (θ_h), vertical displacement of the 1st axle (u_{h1}) and vertical displacement of the 2nd axle (u_{h2}), respectively.

In the case of a coupled approach, the equations of motion of the bridge (Equation (1)) and the vehicle (Equation (2)) are combined into a single equation. Thus, the global mass and stiffness matrices of the system (Equation (7)) are defined by merging the DoFs shared by both sub-systems at each time step. The coupled solution is obtained by applying an integration method such as Wilson-θ to Equation (7). It is worth noting that the time-varying matrices may lead to numerical instability due to singularities associated with very small or close eigenvalues:

$$\begin{bmatrix} M_v & 0 \\ 0 & M_b \end{bmatrix} \cdot \begin{Bmatrix} \ddot{u}_v \\ \ddot{u}_b \end{Bmatrix} + \begin{bmatrix} C_v & C_{vb} \\ C_{bv} & C_b + C_{bb} \end{bmatrix} \cdot \begin{Bmatrix} \dot{u}_v \\ \dot{u}_b \end{Bmatrix} \\ + \begin{bmatrix} K_v & K_{vb} \\ K_{bv} & K_b + K_{bb} \end{bmatrix} \cdot \begin{Bmatrix} u_v \\ u_b \end{Bmatrix} = \begin{Bmatrix} F_r \\ N(-F_g - F_r) \end{Bmatrix} \tag{7}$$

where $[K_{vb}]$, $[K_{bv}]$ and $[K_{bb}]$ are the time-variant stiffness matrices, $[C_{vb}]$, $[C_{bv}]$ and $[C_{bb}]$ are the time-variant damping matrices, and N is a time-variant matrix representing the application of the shape function to the sum of the gravitational forces of the vehicle (F_g) and the interaction forces due to the irregularities of the underlying surface (F_r). Namely, N is an ($n \cdot 1$) column vector, $F_g = m_v \cdot g$ ($g =$ gravity acceleration) and $F_r = k_v \cdot r$, in the case of a single undamped sprung mass model. For a half-car model, N is an ($n \cdot 4$) matrix, while F_g and F_r are ($4 \cdot 1$) column vectors containing the static weight of each axle, and the stiffness of each tire multiplied by the height of the irregularity at its location, respectively. The first two columns of N, as well as the first two elements of F_r and F_g, are zero since they correspond to the DoFs of the half-car related to the body mass.

The time-variant matrices depend on the value and position of the springs and dashpots connecting the vehicle to the bridge. Equation (8) illustrates $\{K_{vb}\}$, $\{K_{bv}\}$, and $[K_{bb}]$ for the scenario in which the sprung mass is located at DoF i, corresponding to the vertical translation of a node in the discretised bridge model. A similar procedure can be applied to obtain the global damping matrix. However, it should be noted that for the models adopted in this paper, no dashpots are considered in the elements connecting the vehicle and the bridge. Hence, $[C_{vb}] = [C_{bv}] = [C_{bb}] = 0$:

$$\begin{bmatrix} K_v & K_{vb} \\ K_{bv} & K_b + K_{bb} \end{bmatrix} = \begin{bmatrix} k_v & 0 & 0 & \cdots & 0 & -k_v & 0 & \cdots & 0 & 0 \\ 0 & k_{1,1} & k_{1,2} & \cdots & k_{1,i-1} & k_{1,i} & k_{1,i+1} & \cdots & k_{1,n-1} & k_{1,n} \\ 0 & k_{2,1} & k_{2,2} & \cdots & k_{2,i-1} & k_{2,i} & k_{2,i+1} & \cdots & k_{2,n-1} & k_{2,n} \\ \vdots & \vdots & \vdots & \ddots & \vdots & \vdots & \vdots & & \vdots & \vdots \\ 0 & k_{i-1,1} & k_{i-1,2} & \cdots & k_{i-1,i-1} & k_{i-1,i} & k_{i-1,i+1} & \cdots & k_{i-1,n-1} & k_{i-1,n} \\ -k_v & k_{i,1} & k_{i,2} & \cdots & k_{i,i-1} & k_{i,i}+k_v & k_{i,i+1} & \cdots & k_{i,n-1} & k_{i,n} \\ 0 & k_{i+1,1} & k_{i+1,2} & \cdots & k_{i+1,i-1} & k_{i+1,i} & k_{i+1,i+1} & \cdots & k_{i+1,n-1} & k_{i+1,n} \\ \vdots & \vdots & \vdots & \ddots & \vdots & \vdots & \vdots & \ddots & \vdots & \vdots \\ 0 & k_{n-1,1} & k_{n-1,2} & \cdots & k_{n-1,i-1} & k_{n-1,i} & k_{n-1,i+1} & \cdots & k_{n-1,n-1} & k_{n-1,n} \\ 0 & k_{n,1} & k_{n,2} & \cdots & k_{n,i-1} & k_{n,i} & k_{n,i+1} & \cdots & k_{n,n-1} & k_{n,n} \end{bmatrix} \tag{8}$$

where $k_{i,j}$ are the elements of the $[K_b]$ matrix plus $[K_{bb}]$, an ($n \cdot n$) matrix for which all elements are equal to zero except for $[K_{bb}]_{i,i} = k_v$; $\{K_{vb}\}$ is a ($1 \cdot n$) row vector and $\{K_{bv}\}$ is a ($n \cdot 1$) column vector. Hence, the global mass and stiffness matrices have dimensions of ($n+1$) · ($n+1$), as a result of adding the number of DoFs in the bridge and sprung mass vehicle model. In general, $\{K_{vb}\}$ and $\{K_{bv}\}$ are ($n_v \cdot n$) and ($n \cdot n_v$) matrices, respectively, where n_v indicates the number of DoFs of the vehicle model. For a half-car, $n_v = 4$. Thus, the global stiffness matrices have dimensions of ($n + n_v$) · ($n + n_v$).

The shape function (N) is used to distribute the gravitational and interaction forces to the affected DoFs of the bridge, which will vary depending on the location of the vehicle axles. Also, if the axle is not positioned exactly over a node, the stiffness of the tire is redistributed to the affected DoFs when creating the time-variant stiffness matrices in Equations (7) and (8). The shape function is equal to zero for the DoFs of the bridge that are not associated with the element where the axle is located and adopts the values in Equation (9) for the DoFs of the element where the axle is located. These values are given as a function of the distance to the left node of the affected element (x_e) and the length of the element (L_e). Each value corresponds to a local DoF of the element following the order established in Figure 1: vertical displacement of the left node (u_1), in-plane rotation of the left node (θ_2), vertical displacement of the right node (u_3) and in-plane rotation of the right node (θ_4):

$$N = \begin{cases} 0 \text{ if } x_a < L_e \cdot (j-1) \\ \begin{Bmatrix} 1 - \dfrac{3 \cdot x_e^2}{L_e^2} + \dfrac{2 \cdot x_e^3}{L_e^3} \\ x_e - \dfrac{2 \cdot x_e^2}{L_e} + \dfrac{x_e^3}{L_e^2} \\ \dfrac{3 \cdot x_e^2}{L_e^2} - \dfrac{2 \cdot x_e^3}{L_e^3} \\ -\dfrac{x_e^2}{L_e} + \dfrac{x_e^3}{L_e^2} \end{Bmatrix} \text{ if } L_e \cdot (j-1) \leq x_a \leq L_e \cdot j \\ 0 \text{ if } x_a > L_e \cdot j \end{cases} \tag{9}$$

where $j = [1, N_b]$ indicates the element number in the discretised model of the bridge, and x_a represents the location of the vehicle axle. In the case of a sprung mass, $x_a = x_v$.

2.2. The uncoupled approach

Coupled methods do not usually require iterating at each time step. In contrast, the uncoupled approach solves Equations (1) and (2) for each sub-system separately, by ensuring compatibility of forces and displacements through an iterative process at each time step. The main advantage is that, while avoiding the singularities exposed before, the matrices of both sub-systems do not change with time and that modal superposition is applicable. Modal superposition can be very relevant in the case of complex models with many degrees of freedom where computational time becomes an issue. The underlying assumption of the uncoupled approach is that the dynamic features of the bridge and the vehicle are independent of each other and remain constant in time. Equation (10) relates the modal coordinates to the displacements of the bridge:

$$\{u_b\} = [\Phi_b] \cdot \{Y_b\} \tag{10}$$

where $\{Y_b\}$ are the modal coordinates of the bridge and $[\Phi_b] = \begin{bmatrix} \{\Phi_1\} & \{\Phi_2\} & \cdots & \{\Phi_{n-2}\} \end{bmatrix}$ is a matrix containing the normalised mode shapes of the bridge.

Each mode shape $\{\Phi_i\}$ corresponds to a column on $[\Phi_b]$ for a total of $n-2$ mode shapes, i.e., the total number of DoFs in the bridge minus the two modes that become irrelevant due to the application of the boundary conditions. After replacing Equation (10) into Equation (1), assuming null damping and pre-multiplying by $[\Phi_b]^t$, the following modal equation is obtained:

$$\{\ddot{Y}_b\} + [\omega_b^2] \cdot \{Y_b\} = [\Phi_b]^t \cdot \{F_b\} \tag{11}$$

where $[\omega_b^2]$ is a diagonal matrix containing the squares of the natural frequencies of the bridge and the superscript t indicates the transpose of a matrix.

The uncoupled approach requires implementing an iterative procedure at each time step to guarantee the compatibility of displacements and forces at the location of the vehicle. Nonetheless, the modal properties of the bridge, i.e., $[\Phi_b]$ and $[\omega_b^2]$, are only calculated once, prior to the first iteration, and they are assumed to remain constant throughout the whole procedure. Figure 2 provides a flow chart detailing these steps for the case of a moving sprung mass. This paper adopts the same stopping criterion as (Green & Cebon, 1997), but extending the check of the relative difference in displacements being less than 2% for consecutive iterations to all the sections along the bridge, i.e., not only to the section holding the maximum displacement.

In both coupled and uncoupled methods, the bending moment at any section of the bridge can be obtained from the displacement record by means of Equation (12) (Pinkaew & Asnachinda, 2007):

$$M(t) = \left(\frac{EI}{L_e^3}\right) \cdot \left\{ (12x_e - 6L_e) \quad L_e(6x_e - 4L_e) \quad -(12x_e - 6L_e) \quad L_e(6x_e - 2L_e) \right\}$$
$$\cdot \begin{Bmatrix} u_{b,i} \\ \theta_{b,i+1} \\ u_{b,i+2} \\ \theta_{b,i+3} \end{Bmatrix} \tag{12}$$

where $u_{b,i}$, $\theta_{b,i+1}$, $u_{b,i+2}$, and $\theta_{b,i+3}$ are the vertical translations and in-plane rotations at the nodes of the element where midspan is located (Figure 1). For the results in subsequent sections, a calculation time step of 0.001 s is employed for both approaches. This small time step accurately captures the frequencies affecting the response of the system without increasing computational time unnecessarily.

3. Impact of a sprung mass on the dynamic properties of a bridge

It is reasonable to assume that a FEM of a bridge will respond differently when integrated with a FEM of a vehicle. Furthermore, given that the location of the vehicle varies at each time step, so will the dynamic features of the system, i.e., the natural frequencies and mode shapes. If an eigenvalue analysis is computed at each time step using the global mass and stiffness matrices from Equation (7), the changes in the dynamic features of the bridge can be characterised. In order to illustrate these changes, typical properties for a reinforced concrete bridge are adopted, i.e., $\rho = 2500 \, \text{kg/m}^3$ and $E = 35 \, \text{GPa}$. Table 1 contains additional characteristics (A = cross-section area; $I = 2^{\text{nd}}$ moment of area) for two structures labelled bridge 'A' and 'B'. The former is assumed to be representative of a short-span bridge with a uniform solid cross-section composed of inverted T-beams. The FEM of bridge 'A' is composed of N_b = 150 elements (L_e = 0.1 m) and $n = 302$ DoFs. The results presented in Section 3 refer exclusively to bridge 'A'.

Figures 3a–c illustrate the evolution of the relative change in $f_{b,1}$, $f_{b,2}$, and f_v respectively, for each location of the sprung mass (x_v) and four different vehicles. These vehicles have the same m_v = 10 tons ($MR = 0.024$) and k_v is adjusted to achieve FR values of 0.25, 1.25, 3.75, and 4.25. These FR values are purposely chosen around $FR = 1$, which entails $f_v = f_{b,1}$, and $FR = 4$, which corresponds to $f_v = f_{b,2}$ for a simply supported beam. The vertical axes in these figures correspond to the relative change in frequencies of the bridge ($\Delta f_{b,i}$) and vehicle (Δf_v), which are calculated according to Equations (13) and (14), respectively:

$$\Delta f_{b,i} = 100 \cdot \frac{f_{bv,i}^j - f_{b,i}}{f_{b,i}} \quad i = 1, 2 \; (\text{mode under consideration}) \tag{13}$$

$$\Delta f_v = 100 \cdot \frac{f_v^j - f_v}{f_v} \tag{14}$$

where $f_{bv,i}^j$ and f_v^j represent the forced frequencies of the bridge and vehicle respectively, when the sprung mass is located at $x_v/L = j$.

Two remarks can be made about the variation of the bridge frequencies:

- The maximum variation of the frequency (in absolute value) will happen when the vehicle is located at the points with maximum modal amplitude, i.e., $x/L = 0.5$ for the 1$^{\text{st}}$ mode (Figure 3a), and $x/L = 0.25, 0.75$ for the 2$^{\text{nd}}$ mode (Figure 3b).
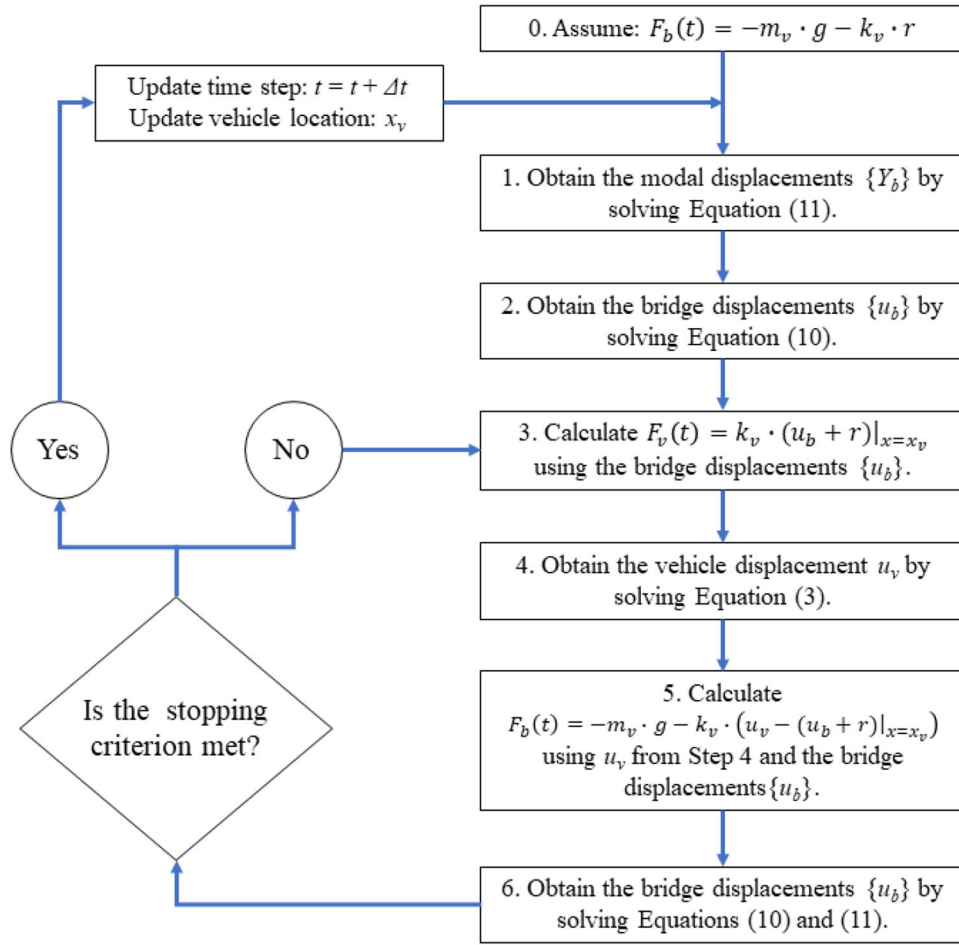
$$0.\ \text{Assume: } F_b(t) = -m_v \cdot g - k_v \cdot r$$

Update time step: $t = t + \Delta t$
Update vehicle location: x_v

1. Obtain the modal displacements $\{Y_b\}$ by solving Equation (11).

2. Obtain the bridge displacements $\{u_b\}$ by solving Equation (10).

Yes   No

3. Calculate $F_v(t) = k_v \cdot (u_b + r)|_{x=x_v}$ using the bridge displacements $\{u_b\}$.

4. Obtain the vehicle displacement u_v by solving Equation (3).

5. Calculate
$$F_b(t) = -m_v \cdot g - k_v \cdot (u_v - (u_b + r)|_{x=x_v})$$
using u_v from Step 4 and the bridge displacements $\{u_b\}$.

Is the stopping criterion met?

6. Obtain the bridge displacements $\{u_b\}$ by solving Equations (10) and (11).

Figure 2. Iterative procedure for the uncoupled approach.

Table 1. Properties of the bridge models.

Label	L (m)	d (m)	A (m²)	m_b (ton)	I (m⁴)	$f_{b,1}$ (Hz)	$f_{b,2}$ (Hz)
'A'	15	0.75	11.25	421.875	0.527	5.656	22.622
'B'	25	1.25	7.34	458.95	1.39	4.091	16.366

- When $FR < 1$ for $f_{b,1}$ (Figure 3a) and when $FR < 4$ for $f_{b,2}$ (Figure 3b), the forced frequency increases compared to the frequency of the bridge in free vibration. Instead, when $FR > 1$ for $f_{b,1}$ (Figure 3a) and when $FR > 4$ for $f_{b,2}$ (Figure 3b), the forced frequency is lower than the free frequency. Generally speaking, the more flexible the vehicle, the stiffer the bridge becomes and vice versa. In other words, the forced frequencies of the vehicle and the bridge tend to compensate for each other.

In the case of the vehicle (Figure 3c), the frequency variation is opposite to that of the bridge:

- For $FR = 0.75$, the value of f_v in forced vibration decreases with respect to free vibration reaching a minimum when the vehicle is located at midspan, i.e., $x_v/L = 0.5$.
- For $FR = 1.25$, there is a gradual increase until the vehicle reaches midspan where a maximum is located; then, the frequency decreases until returning to its value in free vibration when the vehicle leaves the bridge.

- For $FR = 3.75$, the change in f_v is the result of the superposition of two effects: (i) because $FR > 1$, f_v tends to increase similarly to the case of $FR = 1.25$ in Figure 3c; and (ii) because FR < 4, f_v is expected to decrease following a pattern opposite to the one shown for the bridge in Figure 3b for $FR = 3.75$. The combination of these two phenomena leads to a decrease in f_v when the vehicle is around $x_v/L = 0.25$ or $x_v/L = 0.75$, where effect (ii) dominates. On the contrary, f_v raises to a positive variation around midspan, where effects (i) and (ii) are maximum and null, respectively. Thus, for FR values close to 4 and the vehicle located at midspan, f_v may match the value of $f_{b,2}$ in free vibration.
- For $FR = 4.25$, the same reasoning explains the shape of the variation in frequency, although this time both effects are positive given that $FR > 4$, which implies $FR > 1$. Hence, Δf_v is always positive, with maxima when the vehicle is around $x_v/L = 0.25$ or $x_v/L = 0.75$ and a minimum at $x_v/L = 0.5$.

The analysis above has shown how the frequencies vary with the vehicle position for four values of FR and a fixed MR. The results suggest that the value of FR controls whether those variations are positive or negative. The percentage change in frequency of the bridge has been relatively small due to the low mass ratio employed to
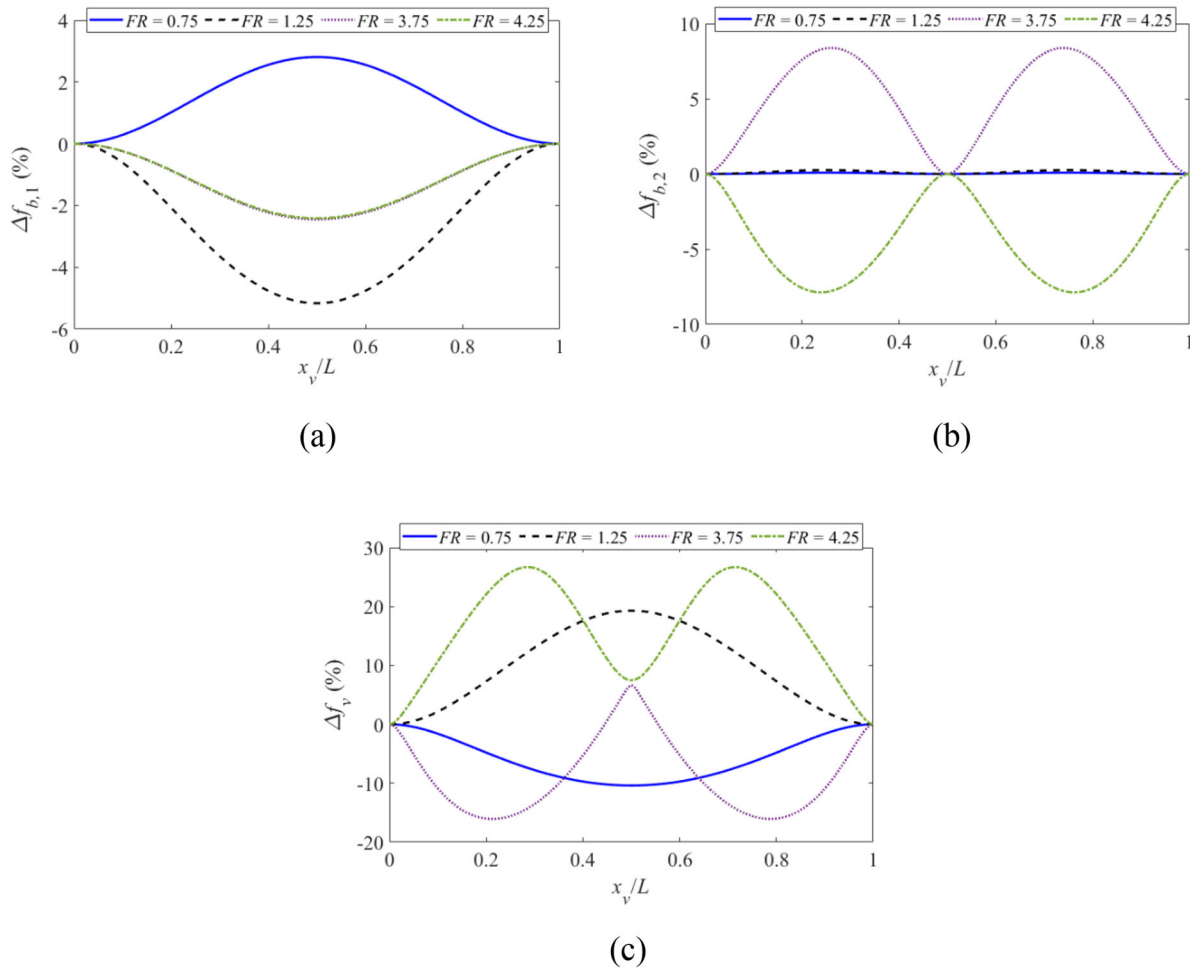
(a)

(b)

(c)

Figure 3. Relative change in frequency vs vehicle location in bridge 'A': (a) 1st mode; (b) 2nd mode; and (c) vehicle.
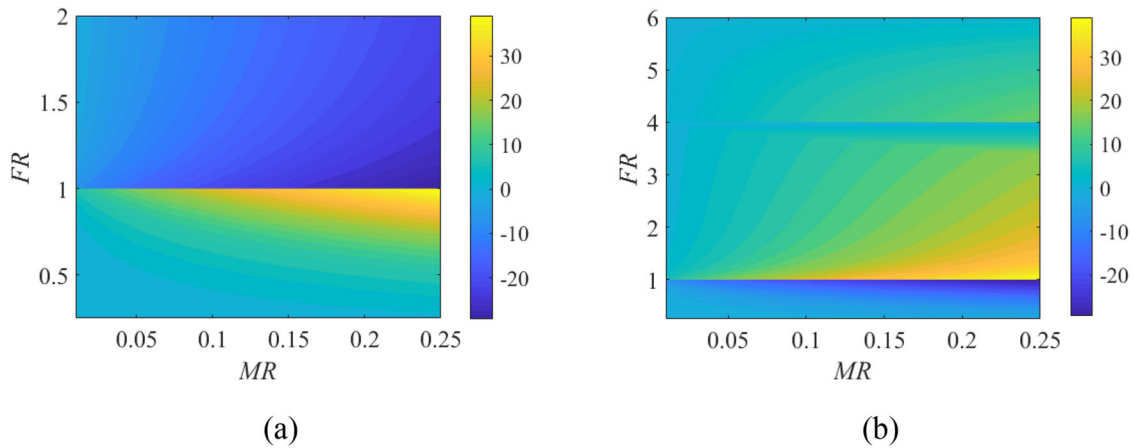

(a)

(b)

Figure 4. Relative change in frequency vs MR vs FR when the vehicle is located at $x_v/L = 0.5$ of bridge 'A' for: (a) 1st mode; and (b) vehicle.

generate these graphs. Although these conclusions have been obtained for bridge 'A', they can be extended to other simply supported bridges with other properties. Next, FR and MR are varied while fixing the sprung mass at the point of maximum modal amplitude for $f_{b,1}$, i.e., midspan. Figures 4a and b show $\Delta f_{b,1}$ and Δf_v respectively; $\Delta f_{b,2}$ is not shown here since it is equal to zero for that position of the vehicle.

The following conclusions can be drawn from Figure 4:

- Overall, as MR increases, the change in the frequencies becomes greater in absolute value. This is felt more strongly when FR tends to 1, in agreement with previous research (Cantero & O'Brien, 2013; Li, Zhu, Law, & Samali, 2020; Yang et al., 2013).
- The contour plots exhibit distinct regions marked by discontinuities corresponding to significant values of FR; namely $FR = 1$ in Figures 4a and b as well as $FR = 4$ in Figure 4b.

- For $FR < 1$:
  - The 1st bridge frequency ($f_{b,1}$) increases (Figure 4a). Changes in MR have a smaller effect on the increment in $f_{b,1}$ than changes in FR, i.e., larger gradients are noticeable in the vertical direction. For $FR \ll 1$, $f_{b,1}$ does not experience variations regardless of the value of MR, i.e., as in the case of a point load model.
  - The vehicle frequency (f_v) decreases (Figure 4b). As expected, the relative variation in f_v is negative, i.e., Δf_v has an opposite sign to $\Delta f_{b,1}$.
- For $FR > 1$:
  - The 1st bridge frequency ($f_{b,1}$) decreases (Figure 4a). Changes in the horizontal axis (MR) have a more pronounced effect on the decrease in $f_{b,1}$ than changes in the vertical axis (FR), i.e., larger gradients appear in the horizontal direction. When FR tends to infinity, $f_{b,1}$ tends to a constant value corresponding to the effect of an unsprung mass.
  - The vehicle frequency (f_v) increases (Figure 4b). The relative change in f_v is always positive when the vehicle is located at midspan, but its value decreases while approaching $FR = 4$. This is due to the interaction with the 2nd mode of the bridge. Even further, Δf_v reaches a constant value when $FR \approx 4$, signalled by horizontal lines in the contour plot. The starting point of these horizontal lines occurs at lower values of FR for higher values of MR. These points correspond to the vehicle frequency in forced vibration exactly matching the 2nd bridge frequency. When FR increases significantly ($FR \gg 4$), Δf_v tends to a constant value regardless of the value of MR.

The mode shapes of the bridge are also affected by the properties and the position of the vehicle. The Modal Assurance Criterion (MAC) is used to compare the mode shapes in forced vibration to the mode shapes in free vibration. Figure 5a shows how the MAC for the first mode shape varies with the vehicle location for the same four vehicles ($MR = 0.024$) as in Figure 3.

Figure 5a suggests that the 1st mode shape barely changes due to the presence of the vehicle, i.e., the minimum MAC value is 0.9999685. While the best match between mode shapes is found when the vehicle is located near the supports or at midspan, there are two locations symmetric to midspan that induce the smallest MAC values. These locations change slightly depending on the values of FR and MR. For instance, Figure 5b gives the MAC values for the 1st mode shape with a fixed $MR = 0.024$ while varying the vehicle location and FR.

For $FR \leq 0.8$ and $FR \geq 1.6$, the mode shape does not experience noticeable changes. For $FR = 0.8$ and $FR = 1.6$, the vehicle location that results in the minimum MAC value appears to be at $x_v/L = 0.3$ (and its symmetrical location at $x_v/L = 0.7$). However, within the range $0.8 < FR < 1.6$, the location of the minimum MAC value, signalled with dashed-dotted lines in Figure 5b, moves from $x_v/L = 0.3$ (or 0.7 in the second half of the bridge) towards the supports when FR tends to 1, reaching values of 0.24 and 0.76 in the

first and second half of the bridge respectively for $FR = 1$. The range of locations occupied by the minimum MAC value becomes wider as MR increases but always leaning towards the support and never towards midspan, i.e., for $MR = 0.24$, the locations for which the minimum MAC value occurs when $FR = 1$ are $x_v/L = 0.22$ and 0.78. On the other hand, the location with the maximum MAC value (the least impact of the vehicle on the mode shape) remains constant at midspan no matter the value of FR (signalled with a dotted line in Figure 5b).

In order to visualise the impact of MR and FR simultaneously, the vehicle position is fixed at a quarter of the span ($x_v/L = 0.25$). Figure 5c plots the MAC values of the 1st mode with respect to those two parameters. As expected, the MAC decreases for larger values of MR and values of FR close to 1. The smallest MAC value of 0.9967 is found for $MR = 0.25$ and $FR = 0.99$.

Using a planar FEM, this section has demonstrated how mass and frequency ratios, as well as the location of the vehicle, can alter the mode shapes and frequencies of a bridge. The impact becomes more significant for high values of MR and values of FR close to 1. These changes are ignored in an uncoupled approach. The sections that follow aim to quantify the errors in the structural response predicted by an uncoupled approach as a function of MR, FR, and the speed of the vehicle.

4. Assessment of errors by the uncoupled method in the case of a sprung mass

The bending moment at midspan is computed using the coupled and uncoupled methods for bridge 'A' and a wide range of FR, MR, and speed values. When using the uncoupled method, all 300 available modes are employed in modal superposition. The consideration of a higher level of discretization in the model and a higher number of modes do not provide noticeable differences with respect to the results reported in this paper. The MR range is defined from 0.01 to 0.25 in increments of 0.01, FR ranges from 0.25 to 4 in increments of 0.01, and the speed is varied from 10 m/s to 40 m/s in intervals of 1 m/s. A MR boundary of 0.01 implies $m_v = 4.219$ tons and a MR boundary of 0.25 results in $m_v = 105.469$ tons. It should be noted that the lower and upper values of the FR range correspond to $f_{v,1}$ values of 1.414 Hz and 22.622 Hz, respectively. A Montecarlo simulation is carried out by randomly sampling values from assumed uniform distributions for MR, FR, and speed. A total of 10^5 cases are analysed, i.e., an average of 4000 cases per MR value, 266 cases per FR value, and 3226 cases per speed value.

4.1. Root mean square error in the estimation of the time-history of bending moment

The accuracy of the uncoupled method is first expressed in terms of the RMSE of the time-varying bending moment at midspan using the coupled method as a reference. The RMSE is calculated according to Equation (15), which
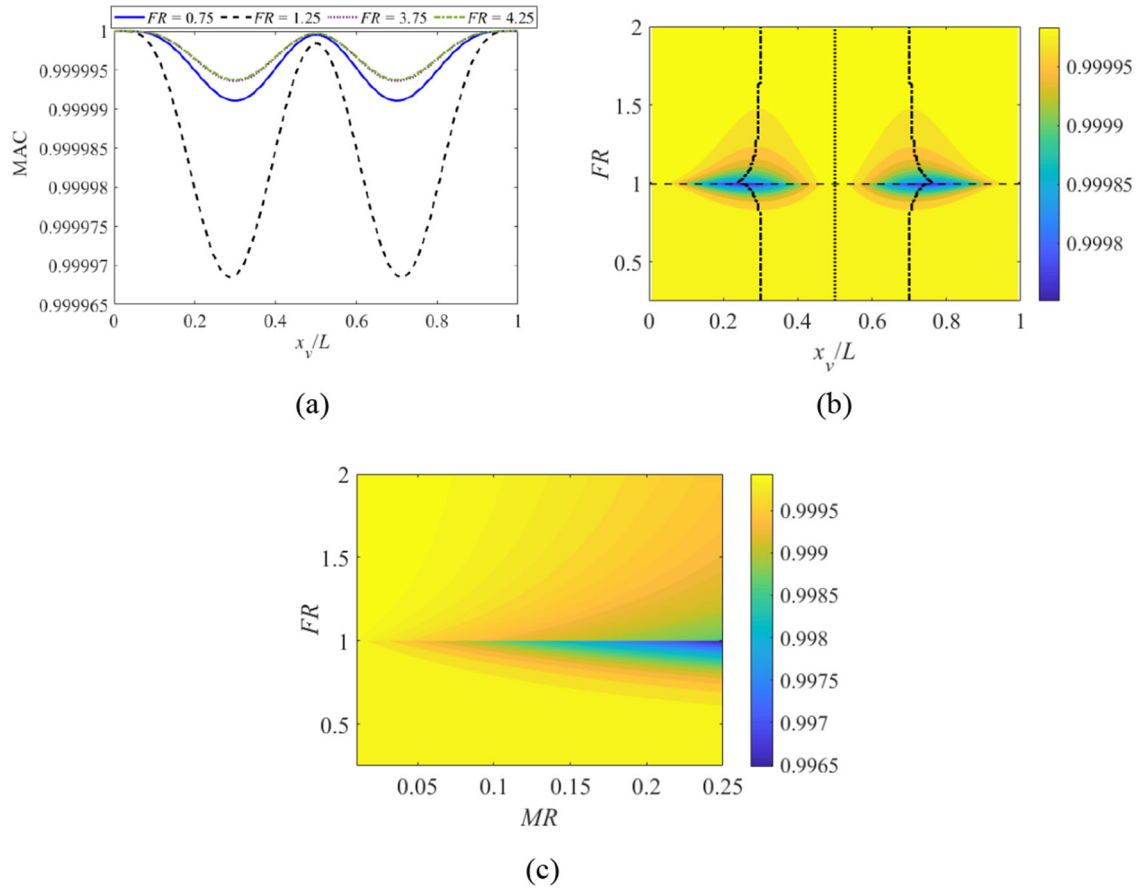
Figure 5. MAC of the 1st mode in bridge 'A': (a) vs vehicle location; (b) vs vehicle location vs FR; and (c) vs MR vs FR.

compares the bending moment at each time step by both methods along the entire bridge length:

$$RMSE = \sqrt{\frac{\sum_{i=1}^{n_t}(M_c^i - M_u^i)^2}{n_t}} \quad (15)$$

where M_c^i = coupled moment at time step i; M_u^i = uncoupled moment at time step i; and n_t = total number of time steps for a specific speed.

Using Equation (16), it is found that the vehicle stiffness k_v varies between $3.33\cdot10^5$ and $2.13\cdot10^9$ N/m for the proposed MR and FR ranges:

$$f_v = \frac{1}{2\pi}\cdot\sqrt{\frac{k_v}{m_v}} \rightarrow k_v = (2\pi\cdot f_v)^2 \cdot m_v$$

$$= (2\pi \cdot FR \cdot f_{b,1})^2 \cdot MR \cdot m_b \quad (16)$$

The terms of the equation for the 1st natural frequency of a simply supported beam can be rearranged to define an equivalent bridge stiffness k_b^*:

$$f_{b,1} = \frac{\pi}{2}\cdot\sqrt{\frac{EI}{m_b\cdot L^3}} \rightarrow \frac{\pi^4 \cdot EI}{L^3} = (2\pi\cdot f_{b,1})^2 \cdot m_b \rightarrow k_b^* = \frac{\pi^4 \cdot EI}{L^3}$$

$$(17)$$

Then, similarly to MR and FR, a ratio of the vehicle to bridge stiffness (SR) can be defined as k_v over k_b^*, which is also analysed. Figure 6 shows the RMSE against FR, MR, SR, and speed.

In the plots in Figure 6, the grey bars represent the mean value of the RMSE for all cases involving a certain value of one parameter and a random value of the others. More specifically, the last bar on the right-hand side of Figure 6b is the result of averaging the RMSE of all cases involving $MR = 0.25$ and any value of speed and FR. The square markers indicate the 5% and 95% percentiles, suggesting that, for a fixed value of one of the parameters, there is high variability in the results depending on the value of the others. In general, the RMSE tends to increase with MR, SR and speed, whereas a local maximum can be observed in Figure 6a for $FR \approx 1$. A clearer picture may be observed by plotting MR, speed and FR in pairs as shown in Figure 7.

Figures 7a–c appear to indicate that high values of MR and speed will lead to larger values of the RMSE, regardless of the FR value. In particular, the largest recorded value of the RMSE (9216.03 N·m) corresponds to the case of $FR = 3.98$, $MR = 0.25$ and speed $= 40$ m/s. Nonetheless, Figures 7a and b still show a small local increment of the RMSE around $FR = 1$, signalled by lighter colours in the contour plots.

The total Sobol indices are employed to quantify the contribution of each variable to the RMSE. The calculation of these indices requires a pseudorandom Montecarlo process where the values of the parameters are shifted according to an established pattern (Sobol, 2001). In this case, specific groups of simulations are selected from the available
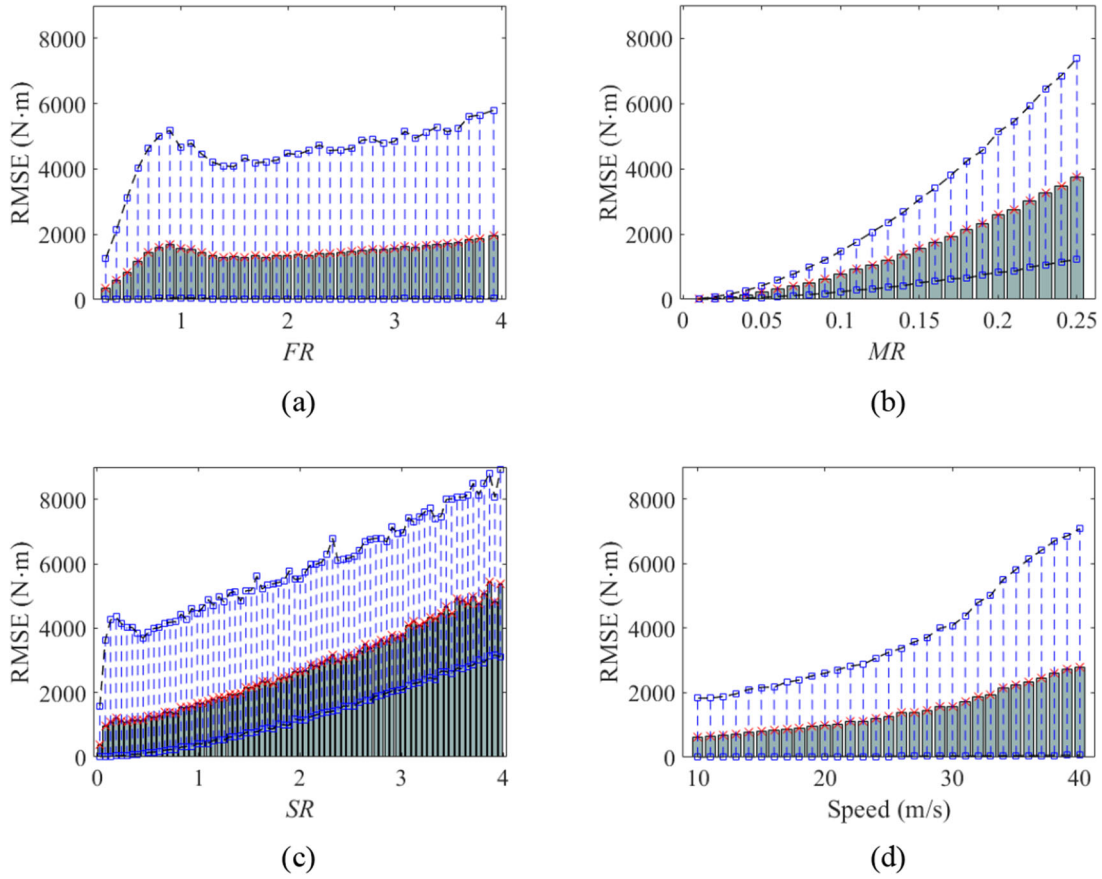
Figure 6. Variation of RMSE (mean, 5 % and 95 % percentiles) in bridge 'A' with (a) *FR*; (b) *MR*; (c) *SR*; and (d) speed.

random set. For the sake of robustness, the indices are computed for five different groups and averaged. The results are 0.69 for *MR*, 0.08 for *FR*, and 0.30 for the speed, supporting the evidence from Figures 6 and 7, by which *MR* has the largest impact followed by the speed and *FR* in the last place.

4.2. Relative error in the estimation of the maximum total moment

RMSE results are relevant for VBI applications such as moving force identification theory, which fully relies on the uncoupled method to predict instantaneous forces from a measured time-history response. As RMSE gets larger, the predicted instantaneous forces will become more inaccurate. However, for other applications, such as the calculation of DAF, the maximum total moment is of more relevance. Therefore, the relative error (%) in the maximum total moment, as defined in Equation (18), is analysed next:

$$e_{t,max} = 100 \cdot \frac{M_{t,u} - M_{t,c}}{M_{t,c}} \tag{18}$$

where $M_{t,c}$ and $M_{t,u}$ represent the total maximum bending moment at midspan for any location of the vehicle according to the coupled and uncoupled methods, respectively. The results are shown in Figure 8.

The impact of *FR* becomes clearly visible in Figures 8a and b where a concentration of high error values can be

observed around $FR = 1$. Figure 8b also indicates that some speeds lead to positive errors (overestimated moments) while others lead to negative ones (underestimated moments) due to the constructive or destructive interference between dynamic and static components of the response. This shows up in Figure 8b in the form of vertical bands that alternate dark and light colours. A similar pattern can be observed in Figure 8c. Furthermore, the presence of negative and positive values for different speeds explains the low error values displayed in Figure 8a given that each point (i,j) of the contour plot corresponds to the average of all the $e_{t,max}$ values for FR_i, MR_j and any speed. Overall, the maximum recorded value of $e_{t,max}$ is 0.54% for the case of $FR = 0.86$, $MR = 0.25$ and speed = 40 m/s.

The total Sobol indices are again used to quantify the significance of each parameter. In the case of $e_{t,max}$, values of 0.22, 0.21, and 0.89 are found for *MR*, *FR*, and speed, respectively. The largest index corresponds to the speed, whereas the contribution of *MR* and *FR* is roughly similar. In contrast with the RMSE, the speed gains influence while *MR* has a lesser impact on $e_{t,max}$. The effect of the speed on $e_{t,max}$ is further explored in Figure 8d. Although the trend of the absolute value of the error is to increase as the speed increases, there is a series of peaks and throughs that tend to be more pronounced as speed increases. As a result, there are certain speeds for which the uncoupled method would be less conservative than the coupled one, namely in the range between 23 and 30 m/s (Figure 8d).
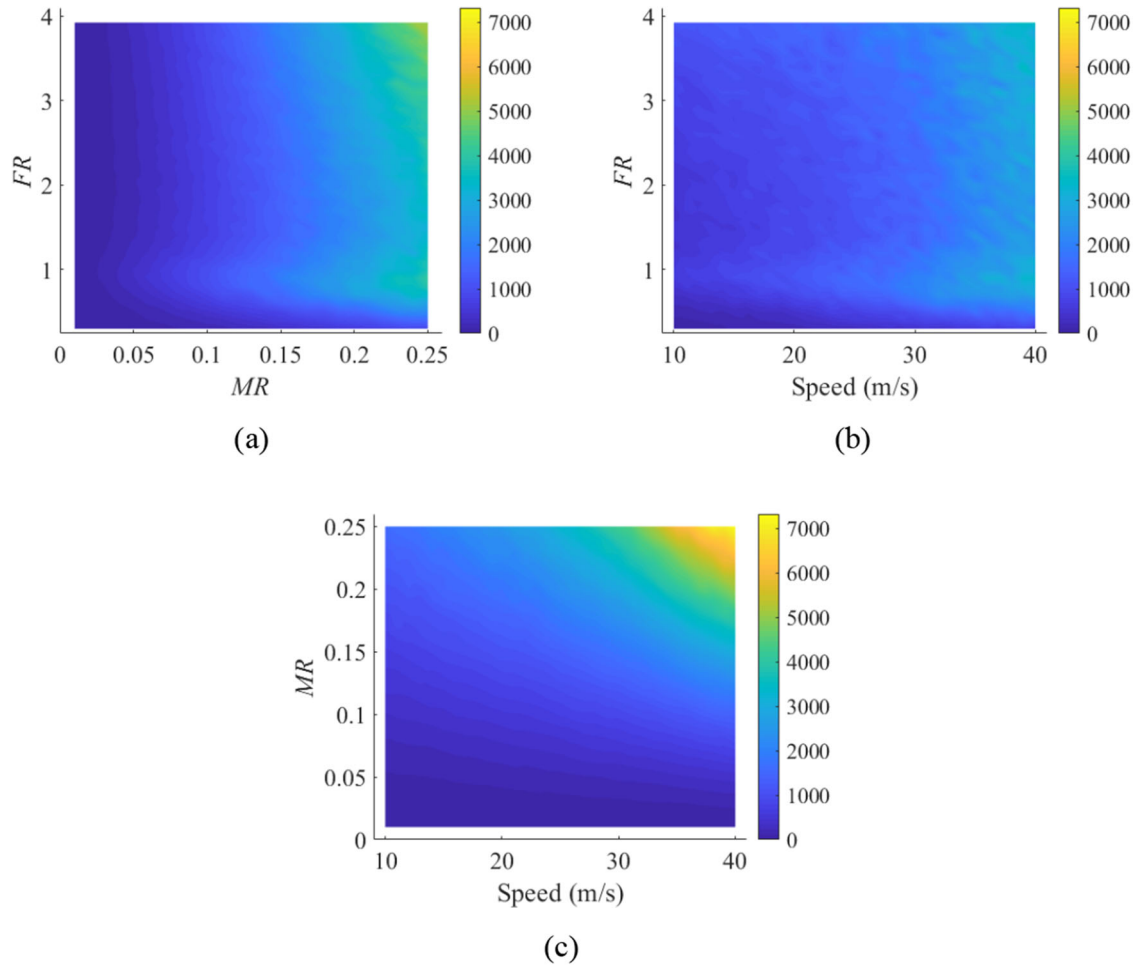
Figure 7. Variation of RMSE in bridge 'A' vs (a) *FR* and *MR*; (b) *FR* and speed; (c) *MR* and speed.

4.3. Impact of a longer span on errors

A second bridge, namely bridge 'B', is analysed to evaluate the impact of the increased span length on the performance of the uncoupled method. The properties of bridge 'B', given in Table 1, are adopted to be representative of a typical medium-span concrete bridge. The cross-section is based on a series of Y beams supporting a thin slab. The FEM of bridge 'B' is discretised into 250 elements 0.1 m long each, and the total number of DoFs is $n = 502$. When using the uncoupled method and modal superposition, all 500 modes are taken into consideration.

The second set of 10^5 Montecarlo simulations are carried out with the parameters (*MR*, *FR*, and speed) varying in the same ranges as for bridge 'A'. In this case, the resulting minimum and maximum values are 4.59 and 114.74 tons, 1.02 and 16.37 Hz, $1.9 \cdot 10^5$ and $1.21 \cdot 10^9$ N/m for m_v, f_v, and k_v, respectively. Figures 9a and b compare the results from bridges 'A' and 'B' in terms of the RMSE and $e_{t,max}$, respectively. Figure 9c allows comparing the evolution of the average value of the coupled moment, $M_{t,c}$, against the evolution of the RMSE with respect to *MR*.

The histograms show how the distributions of the RMSE (Figure 9a) and $e_{t,max}$ (Figure 9b) are similar for both bridges but, while the former is almost identical (slightly smaller mean values for bridge 'B'), the latter is quite narrower for bridge 'B'. The values of $e_{t,max}$ vary between − 0.16% and 0.19% for

bridge 'B' as opposed to − 0.25% and 0.54% for bridge 'A'. In Figure 9c, it can be seen that the RMSE vs *MR* curve is similar for both bridges, except for the highest *MR* values. Therefore, the coupled moment is much larger for bridge 'B' than for bridge 'A' regardless of the value of *MR*. Given that the $e_{t,max}$ is computed as the relative difference between the uncoupled and coupled methods (Equation (18)), the lower values of $e_{t,max}$ for bridge 'B' can be attributed to a larger value of the denominator than bridge 'A', while the difference in the numerator by both bridges changes to a lesser extent.

5. Assessment of errors by the uncoupled method in the case of a half-car

A set of 10^5 Montecarlo simulations are carried out on bridge 'A' by randomly varying the properties of the vehicle and its speed. The properties of the tires (k_{t1}, k_{t2}), suspensions (k_{s1}, c_{s1}, k_{s2}, c_{s2}) and axle masses (m_1, m_2) are taken from Cantero and Gonzalez (2015). The variables are assumed to follow normal distributions truncated by minimum and maximum values. Similarly, the mass moment of inertia (I_3) of the body mass is sampled from a normal distribution in which the parameters have been slightly modified from Cantero and Gonzalez (2015) to be consistent with the values of the body masses. The parameters of the normal distributions for these seven variables are provided
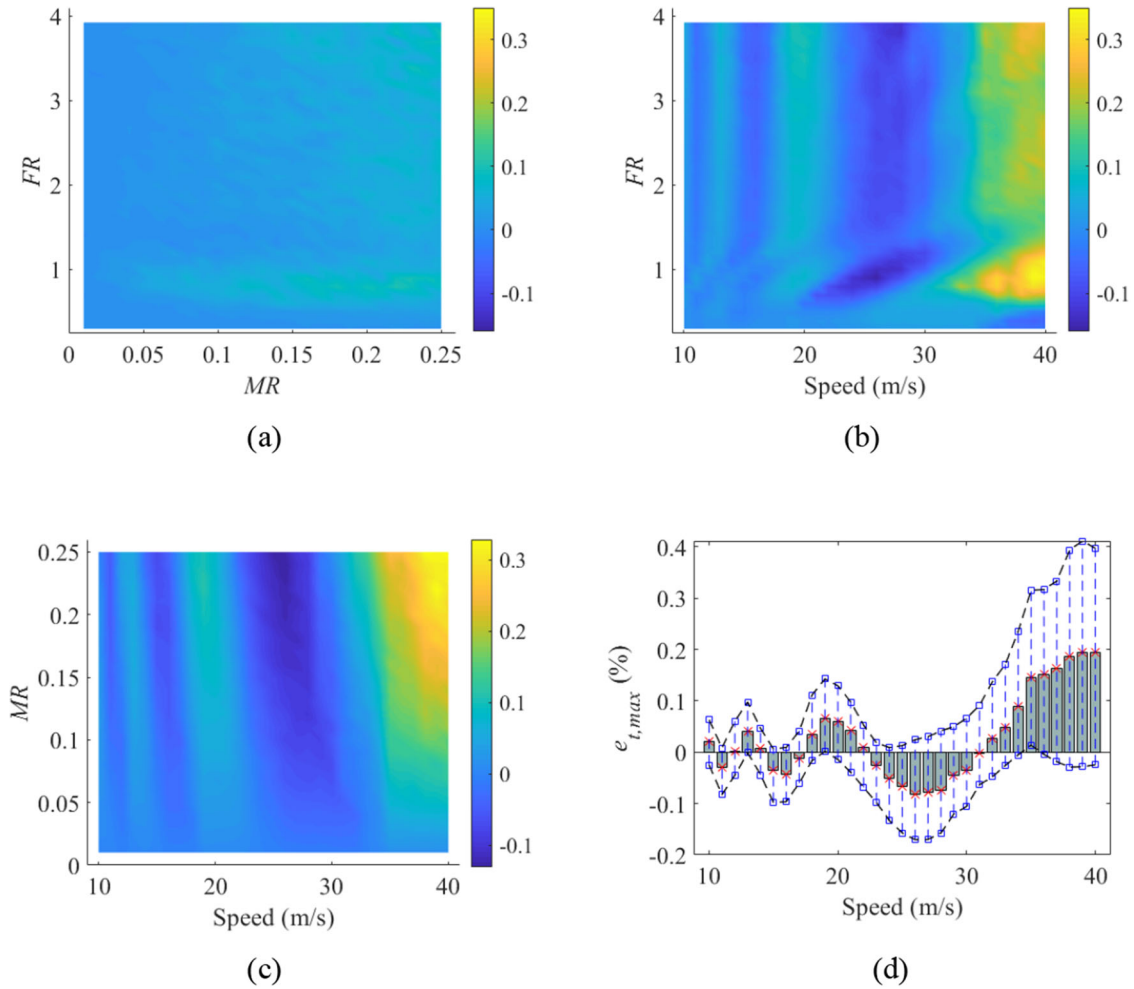
Figure 8. Variation of $e_{t,max}$ (%) in bridge 'A' vs (a) FR and MR; (b) FR and speed; (c) MR and speed; (d) speed.

in Table 2. The values of the spacing (s) are sampled from a uniform distribution ranging from 3 m to 7 m in intervals of 0.1 m, to allow for an analysis of this variable similar to the one conducted in Section 4 with MR, FR, and the vehicle speed.

In order to facilitate the comparison of the results obtained in this section with those shown in Sections 4.1 and 4.2, the same values of the vehicle speed and MR covered by the sprung mass are used for the half-car. Hence, the value of the body mass (m_3) for each simulation is calculated by assuming that MR corresponds to the ratio between the total mass of the vehicle ($m_3 + m_1 + m_2$) and the mass of the bridge. As a result, the value of m_3 ranges from 427.88 kg to 104.46 tons, the former corresponding to a scenario with $MR = 0.01$ and large axle masses, and the latter to $MR = 0.25$ and values of the axle masses close to their minimum value. Finally, there are four frequencies associated with the half-car, and it is not possible to define a value of FR equivalent to the one employed for the sprung mass. Alternatively, the results are analysed in terms of the frequency ratio associated with the vehicle speed, s and $f_{b,1}$, namely:

$$FR_s = \frac{speed}{s \cdot f_{b,1}} \tag{19}$$

5.1. Root mean square error in the estimation of the time-history of bending moment and relative error (%) in the estimation of the maximum total moment

The RMSE is calculated according to Equation (15) and plotted in Figures 10a–c with respect to MR, speed and FR_s. Figures 10a and b can be directly compared with Figures 6b and d. Although the trends in Figures 10a and 6b are similar, the magnitude of the RMSE is significantly smaller in the case of the half-car. When evaluating the results in terms of the vehicle speed, there is no apparent trend in the case of the half-car (Figure 10b), as opposed to the smoothly increasing values of RMSE associated with higher speeds in the case of the sprung mass (Figure 6d).

However, the new parameter FR_s related to the spacing between the axles of the half-car reveals an underlying trend (Figure 10c). Local maxima can be identified when an exact number of harmonics of the pseudo-frequency given by axle spacing and speed fits the duration of the main harmonic of the bridge (i.e., $f_{b,1} = p \cdot speed/s$ with $p = 1, 2, 4$). A global maximum can be seen in Figure 10c around $FR_s = 1$, which corresponds to values of speed and spacing that result in a frequency that matches $f_{b,1}$. In that sense, this phenomenon resembles the one observed in Figure 6a, where the RMSE is plotted as a function of FR.
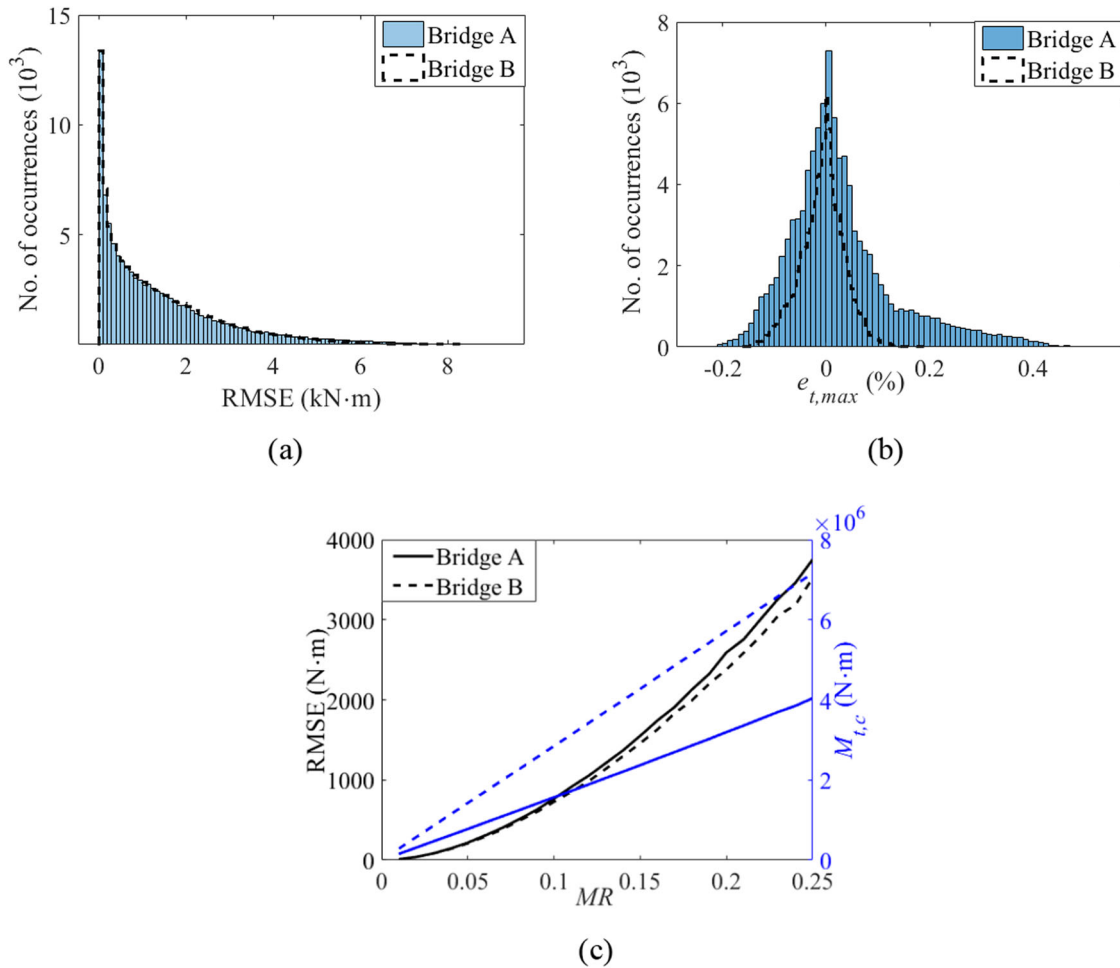
(a)

(b)

(c)

Figure 9. Comparison of results for bridges 'A' and 'B': (a) RMSE histogram; (b) $e_{t,max}$ histogram; and (c) evolution of RMSE and $M_{t,c}$ with MR.

Table 2. Properties of the half-car.

Property	Mean	Standard deviation	Minimum	Maximum	Units
Tire stiffness (k_{t1}, k_{t2})	10^6	$3 \cdot 10^5$	$5 \cdot 10^5$	$2 \cdot 10^6$	N/m
Suspension stiffness (k_{s1}, k_{s2})	10^6	$3 \cdot 10^5$	$5 \cdot 10^5$	$2 \cdot 10^6$	N/m
Suspension damping (c_{s1}, c_{s2})	10^4	3000	5000	$2 \cdot 10^4$	N·s/m
Axle masses (m_1, m_2)	1000	500	500	2000	kg
Mass moment of inertia (I_3)	$5 \cdot 10^5$	10^5	$8 \cdot 10^4$	10^6	kg·m²

Regarding the values of the relative error ($e_{t,max}$), they are significantly smaller for the half-car than for the sprung mass. While $e_{t,max}$ acquires a maximum value of 0.54% in Section 4.2, the maximum recorded value in simulations with the half-car is only 0.03%, i.e., around 16 times less. No remarkable trend has been found between $e_{t,max}$, and MR or speed. The behaviour between $e_{t,max}$ and FR_s, shown in Figure 10d, is similar to the one exhibited by the RMSE in Figure 10c. Figure 10d shows negative values for $e_{t,max}$ when $FR_s \approx 2$, implying a slight underestimation of the maximum bending moment by the uncoupled method that was not visible in Figure 10c. It is worth noting that the local maxima at $FR_s \approx 0.25$ and 0.5 are more prominent than the one located at $FR_s \approx 1$, which may indicate that combinations of s and vehicle speed leading to an even exact number of cycles associated with $f_{b,1}$ may be critical as well. In any case, the magnitude of the errors can be considered insignificant.

5.2. Impact of a road profile on errors

Previous analysis has been restricted to the impact that vehicle and bridge parameters have on the accuracy of the uncoupled method. Nonetheless, it is often that a road profile is included in the transient simulation to recreate a more realistic scenario. For that purpose, the error of the uncoupled model is evaluated here when a road profile is introduced. A class 'B' road roughness is simulated according to the ISO standard 8608:2016.

The analysed scenarios are the same as in Section 5.1 in terms of the vehicle parameters, but the geometric mean of the road is randomly varied following a uniform distribution between $32 \cdot 10^{-6}$ and $128 \cdot 10^{-6}$ m³. The latter values represent the lower and upper limits of class 'B' roads according to ISO 8608:2016, respectively. In approximately 7.5% of the performed simulations, the vehicle loses contact with the surface due to significant road irregularities. The affected simulations are removed from the analysis to place focus only upon scenarios with permanent contact between vehicle and bridge. Figure 11 shows the errors of the uncoupled method according to the same parameters presented in Figure 10.

Figure 11a indicates that, although the trend of the RMSE increasing with MR is still present in the data, it is not as significant as in Figure 10a. On the other hand, Figure 11b
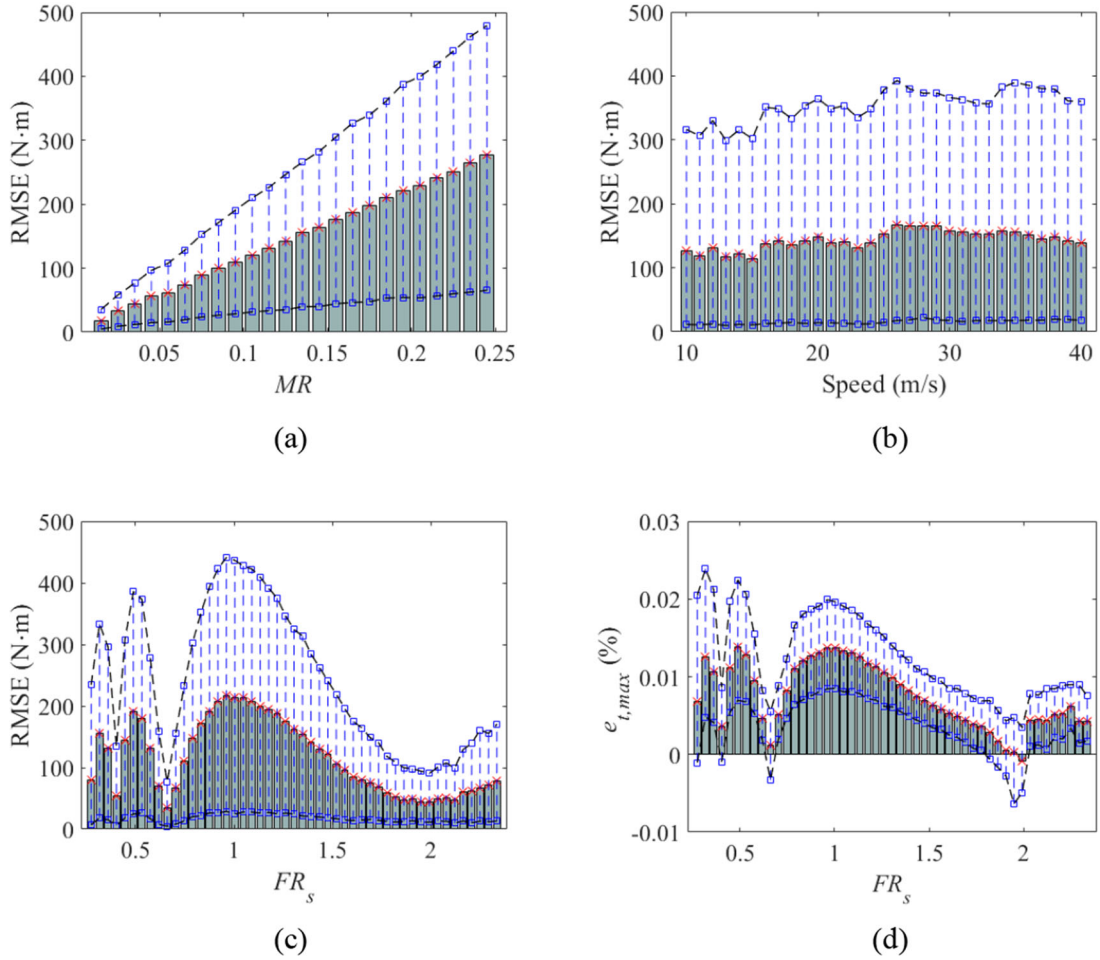
Figure 10. Variation of errors in bridge 'A' for a half-car: RMSE (mean, 5 % and 95 % percentiles) with (a) MR; (b) speed; and (c) FR_s; (d) $e_{t,max}$ (%) with FR_s.

presents a clear tendency of the RMSE to increase with speed that is not visible in Figure 10b. The trend here is more similar to that of Figure 6d corresponding to the sprung mass. Although local maxima can be observed around $FR_s \approx 0.5$ and 1 in Figure 11c, the introduction of the road profile seems to govern the response and to mask the pattern previously identified in Figure 10c. Finally, the presence of the road profile significantly modifies the distribution of $e_{t,max}$ with FR_s. It can be seen that not only the trend is lost, but the results show a high variability for a given value of FR_s, which can be identified in Figure 11d by wider ranges between the 5% and 95% percentiles.

Figure 12a provides the distribution of $e_{t,max}$ with respect to MR in the absence of a road profile, where errors are trivial and no obvious pattern is noted. Conversely, a trend arises in the presence of a class 'B' road roughness, with mean values of $e_{t,max}$ close to zero due to the combination of positive and negative errors for different speeds, while the range between percentiles decreases significantly as MR increases. It is important to emphasise that the values plotted in Figure 12a are significantly smaller than in Figure 12b.

6. Discussion

The results presented in Section 4 corresponding to the sprung mass indicate that the uncoupled and coupled

approaches show good agreement on the results. Nonetheless, the following trends in RMSE are noted as a function of the vehicle parameters:

- FR (Figure 6a) induces a non-monotonic evolution of the RMSE. Initially, the mean value of the RMSE increases from 341.5 to 1694 N·m as FR tends to 1. The error of the uncoupled method becomes larger as the frequencies and mode shapes of the system in forced vibration differ more significantly from those of the individual vehicle and bridge in free vibration, as described in Section 3. Then, the RMSE decreases slightly as FR increases beyond 1. The latter is due to smaller variations in the frequencies and mode shapes as compared to $FR \approx 1$. However, the RMSE slowly starts to increase again when reaching $FR \approx 1.4$ and continues increasing for the remaining of the FR range. The reasons are twofold: (i) the variation of the 1st bridge frequency tends to a constant value for $FR \gg 1$ (Figure 4a), causing a certain RMSE even far apart from $FR = 1$; and (ii) as FR tends to 4, the 2nd bridge mode starts to be affected, which in turn contributes to an increase of the RMSE. Nevertheless, these changes are small and the mean value of RMSE remains below 2000 N·m for the entire range under consideration.
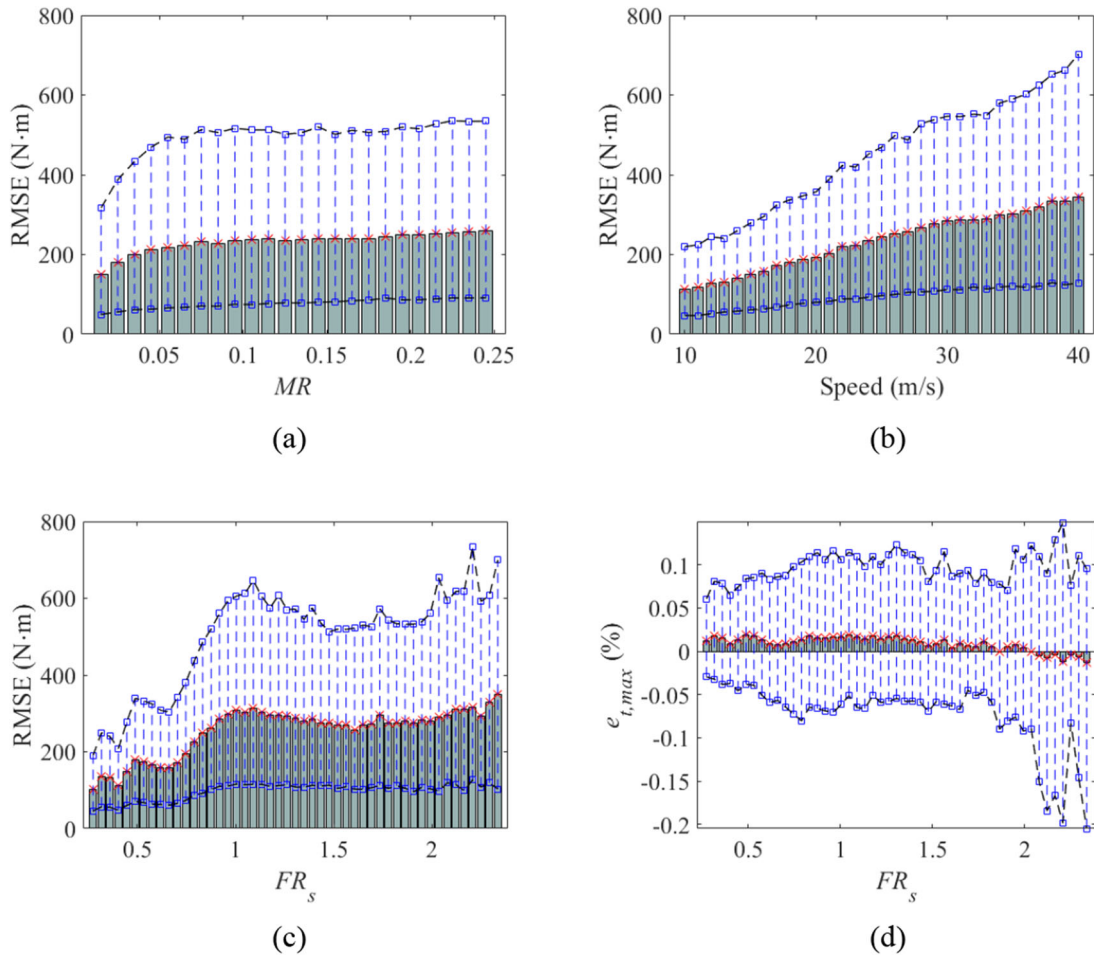
Figure 11. Variation of errors in bridge 'A' for a half-car travelling over a class 'B' road profile: RMSE (mean, 5 % and 95 % percentiles) with (a) MR; (b) speed; and (c) FR_s; (d) $e_{t,max}$ (%) with FR_s.
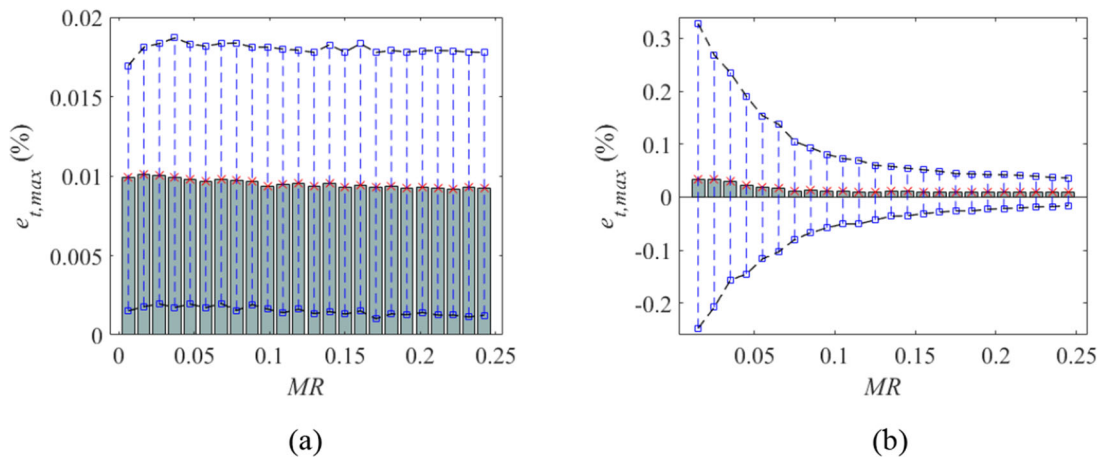

Figure 12. Variation of $e_{t,max}$ (%) with MR (mean, 5 % and 95 % percentiles) in bridge 'A' for a half-car travelling over: (a) a smooth profile; and (b) a class 'B' road profile.

- MR (Figure 6b) is the parameter causing the largest impact on the RMSE as confirmed by Sobol indices, i.e., more than twice influential than speed and close to nine times more influential than FR. In contrast with FR, a mean RMSE value of 2000 N·m is exceeded for $MR = 0.18$ and any other larger MR value, and a maximum mean value of 3752 N·m is reached at the upper end of the range ($MR = 0.25$). The lowest values of MR

hardly have any influence on the RMSE, but from $MR = 0.05$, RMSE grows steadily with MR. The width of the confidence interval marked by the percentiles also becomes wider as MR increases, which is to be expected given the increase in non-stationarity of the system.

- SR (Figure 6c) reflects the combined effects of MR and FR. Hence, the RMSE rapidly grows for low values of SR, corresponding to $FR \approx 1$ and the whole range of

MR, until reaching a maximum value of 1197 for $SR = 0.19$. Then, the RMSE evolution flattens for a short range of *SR* values before starting to increase again, in a similar manner to Figure 6b, but unlike Figure 6b, the width of the 95% confidence interval increases only slightly with *SR*.

- The vehicle speed does not change frequencies or mode shapes, but it affects the relative position of the vehicle with respect to the mode shape. The mean value of the RMSE (Figure 6d) increases approximately linearly with speed until reaching 1584 N·m at 30 m/s. Between 33 and 40 m/s, the curve becomes steeper reaching a maximum mean RMSE value of 2788 N·m at the upper end.
- When increasing the span length of the bridge from 15 to 25 m, the differences in RMSE are undistinguishable for *MR* below 0.1 and above that value, differences between both bridges increase gradually with higher *MR*, being the 15 m bridge the most inaccurate (Figure 9c).

Regarding $e_{t,max}$, the vehicle speed is by far the most influential parameter according to Sobol indices. Some nuance on why errors are amplified for certain speed ranges is gathered from the variation of $e_{t,max}$ with speed (Figure 8d). This variation resembles the pattern of the DAF versus speed (Brady, O'Brien, & Žnidarič, 2006; González, Cantero, & OBrien, 2011; Gonzalez et al., 2010). As expected, when the maximum total moment is approximately equal to the maximum static moment, i.e., DAF $\approx$ 1, errors are minimal. These errors increase with a larger difference between the maximum total moment and maximum static moment, i.e., the farther apart DAF is from 1. The highest speeds tend to increase DAF and these differences and, as a result, lead to the most significant errors. It must be highlighted that although the uncoupled method is usually more conservative than the coupled method, there are certain ranges of speed where this is not true. Broadly speaking, these ranges belong to combinations of the oscillatory dynamic component around the static component of the response that reduce the maximum total moment.

In the absence of a road profile, the analysis of the results corresponding to a half-car conducted in Section 5 provides distinct differences with previous results from Section 4:

- The magnitude of the errors, both in terms of the RMSE and $e_{t,max}$ is significantly smaller for the same values of *MR*. The maximum value of RMSE is 696.14 N·m for $MR = 0.25$, speed = 36 m/s and $FR_s = 0.98$, whereas the maximum value of $e_{t,max}$ adds up to 0.034% for $MR = 0.25$, speed = 10 m/s and $FR_s = 0.34$. Thus, a more complex vehicle model does not result in larger errors of the uncoupled method, rather it seems that the effect of concentrating the mass in a single point, as it is the case of the sprung mass model, leads to a larger moment and it is more detrimental.
- The harmonic effect of speed identified in Figure 8d for $e_{t,max}$ in the case of the sprung mass is no longer visible with the half-car. Instead, the pseudo-frequency related

to the axle spacing becomes relevant and provides a similar pattern as exemplified by Figures 10c and d regarding the RMSE and the $e_{t,max}$, respectively. Hence, critical scenarios can be identified when the pseudo-frequency matches $f_{b,1}$ or an integer multiple.

The introduction of a rough class 'B' road profile has several effects:

- The impact of the speed (Figure 11b) on the RMSE becomes more relevant than the impact of *MR* (Figure 11a), which can be attributed to the road profile amplifying the dynamic effect of the vehicle traversing the bridge and reducing the significance of the static component associated with the mass of the vehicle.
- The trends previously identified in the absence of a road profile (Figure 10) cannot be recognised anymore. However, a new trend can be visualised in Figure 12b corresponding to the evolution of $e_{t,max}$ with respect to *MR*. The dynamic excitation induced by the road profile potentially leads to larger errors in the case of low *MR* values due to a combination of a large dynamic component of the moment relative to a small static moment. It is well established in the literature that for a given road profile, DAF decreases as the *MR* increases (Cantero et al., 2011; Caprani, Gonzalez, Rattigan, & OBrien, 2012; Gonzalez, Rattigan, et al., 2008; OBrien, Cantero, Enright, & Gonzalez, 2010). The dynamic component of the total moment may increase with *MR*, but normally not to the same extent as the static component. In line with these findings, the relative error in $e_{t,max}$ tends to decrease for higher vehicular masses.
- The error of the uncoupled method increases both in terms of the RMSE and $e_{t,max}$, although values as significant as those of the sprung mass are not achieved. The uncoupled method is less conservative (i.e., the bending moment is underestimated) for a significantly larger number of cases in the presence of a class 'B' rough profile (Figure 11d) compared to a smooth profile (Figure 10d).

7. Conclusions

Existing VBI-based research typically uses either the coupled or the uncoupled approach, but unlike the current paper, results by both approaches are not provided together. Even further, when a publication uses an uncoupled approach, the error incurred is usually omitted or assumed to be very small. Indeed, this error is likely to be negligible for some scenarios or applications, but this paper has shown that the latter cannot be generalised since it all depends on the vehicular parameters and how they interact with the bridge properties.

This gap in the literature has been addressed here by assessing two error estimates: (i) the overall differences in the time-history response by coupled and uncoupled methods via the RMSE, and (ii) the relative inaccuracies associated with the maximum total moment via $e_{t,max}$. These

errors exist due to the assumption of the uncoupled method that mode shapes and frequencies of the bridge do not change with the load crossing it. The suitability of the uncoupled method for solving VBI problems has been tested for a moving load with properties varied according to its mass ratio (MR), frequency ratio (FR), and speed, travelling over two different span lengths. A simple sprung mass has been shown to provide a conservative estimate of the errors found for a half-car.

All available mode shapes have been considered for the calculations of modal superposition to ensure errors were purely due to differences between uncoupled and coupled methods as opposed to the use of an insufficient number of modes. Overall, the uncoupled method has not incurred in significant errors when compared to the coupled method for the range of values under investigation. Nonetheless, the performance of the uncoupled method has been observed to degrade in two situations. Firstly, when FR is close to 1, although this has generally led only to a small local maximum of the error indicators. This phenomenon is related to the change in forced frequencies and mode shapes made evident through eigenvalue analysis. When dealing with a half-car, results have been sensitive to a new FR_s parameter that measures how vehicle spacing and speed interact with the main frequency of the bridge. Secondly, the errors have been shown to increase as the MR and speed acquire larger values.

Two general remarks can be made regarding the impact of speed: (i) the uncoupled method tends to be conservative with respect to the coupled method for the fastest speeds, which lead to the highest errors; and (ii) the errors are noticeably small for the ranges being considered. While the trends observed in the absence of a road profile are foreseen to remain for smooth road profiles, the randomness of a class 'B' roughness has modified patterns and increased errors significantly, i.e., the confidence intervals have widened by approximately one order of magnitude and have masked any underlying trend related to the speed.

In short, larger dynamic moments, due to larger vehicular dynamic forces as a result of a higher MR, a higher speed, some sort of frequency matching, a rougher profile, or a combination of these factors, will lead to a larger RMSE by the uncoupled method. Lighter vehicles travelling over a rough profile are prone to higher DAF, i.e., a higher percentage of dynamic component making the total moment, and consequently, $e_{t,max}$ has been shown to become less relevant as MR increases for a class 'B' road profile. Finally, higher speeds and MR than the ones tested here are attainable in real scenarios such as high-speed trains, which could potentially lead to more significant errors than the ones reported in this paper. Further research is needed to generalise this concept allowing for situations with a higher degree of non-stationarity and non-linearity, such as higher mass ratios, and non-linear bridge and vehicle elements.

Disclosure statement

No potential conflict of interest was reported by the authors.

ORCID

Arturo González (iD) http://orcid.org/0000-0003-4942-1255
Enrique Covián (iD) http://orcid.org/0000-0001-6476-4817
Miguel Casero (iD) http://orcid.org/0000-0001-9248-8231

Data availability statement

The data that support the findings of this study are available from the corresponding author, M.C., upon reasonable request.

References

Brady, S. P., O'Brien, E. J., & Žnidarič, A. (2006). Effect of vehicle velocity on the dynamic amplification of a vehicle crossing a simply supported bridge. *Journal of Bridge Engineering*, 11(2), 241–249. doi:10.1061/(ASCE)1084-0702(2006)11:2(241)

Cantero, D., & Gonzalez, A. (2015). Bridge damage detection using weigh-in-motion technology. *Journal of Bridge Engineering*, 20(5), 04014078. doi:10.1061/(ASCE)BE.1943-5592.0000674

Cantero, D., Gonzalez, A., & OBrien, E. J. (2011). Comparison of bridge dynamic amplifications due to articulated 5-axle trucks and large cranes. *The Baltic Journal of Road and Bridge Engineering*, 6(1), 39–47. doi:10.3846/bjrbe.2011.06

Cantero, D., González, A., & Obrien, E. J. (2009). Maximum dynamic stress on bridges traversed by moving loads. *Proceedings of the Institution of Civil Engineers - Bridge Engineering*, 162(2), 75–85. doi:10.1680/bren.2009.162.2.75

Cantero, D., Hester, D., & Brownjohn, J. (2017). Evolution of bridge frequencies and modes of vibration during truck passage. *Engineering Structures*, 152, 452–464. doi:10.1016/j.engstruct.2017.09.039

Cantero, D., McGetrick, P., Kim, C. W., & OBrien, E. (2019). Experimental monitoring of bridge frequency evolution during the passage of vehicles with different suspension properties. *Engineering Structures*, 187, 209–219. doi:10.1016/j.engstruct.2019.02.065

Cantero, D., & O'Brien, E. J. (2013). The non-stationarity of apparent bridge natural frequencies during vehicle crossing events. *FME Transactions*, 41, 279–284.

Cantero, D., Ulker-Kaustell, M., & Karoumi, R. (2016). Time-frequency analysis of railway bridge response in forced vibration. *Mechanical Systems and Signal Processing*, 76–77, 518–530. doi:10.1016/j.ymssp.2016.01.016

Caprani, C. C., Gonzalez, A., Rattigan, P. H., & OBrien, E. J. (2012). Assessment dynamic ratio for traffic loading on highway bridges. *Structure and Infrastructure Engineering*, 8(3), 295–304. doi:10.1080/15732471003667645

Chan, T. H. T., Yu, L., Law, S. S., & Yung, T. H. (2001). Moving force identification studies, I: Theory. *Journal of Sound and Vibration*, 247(1), 59–76. doi:10.1006/jsvi.2001.3630

Chang, K. C., Kim, C. W., & Borjigin, S. (2014). Variability in bridge frequency induced by a parked vehicle. *Smart Structures and Systems*, 13(5), 755–773. doi:10.12989/sss.2014.13.5.755

Deng, L., Yu, Y., Zou, Q. L., & Cai, C. S. (2015). State-of-the-art review of dynamic impact factors of highway bridges. *Journal of Bridge Engineering*, 20(5), 04014080. doi:10.1061/(ASCE)BE.1943-5592.0000672

Feng, K., González, A., & Casero, M. (2021). A kNN algorithm for locating and quantifying stiffness loss in a bridge from the forced

vibration due to a truck crossing at low speed. *Mechanical Systems and Signal Processing, 154*, 107599. doi:10.1016/j.ymssp.2020.107599

Fryba, L. (1999). *Vibration of solids and structures under moving loads* (3rd ed.). London: Thomas Telford.

González, A. (2010). Vehicle-bridge dynamic interaction using finite element modelling. In D. Moratal (Ed.), *Finite element analysis* (p. 26). IntechOpen. doi:10.5772/10235

González, A., Cantero, D., & OBrien, E. J. (2011). Dynamic increment for shear force due to heavy vehicles crossing a highway bridge. *Computers & Structures, 89*(23–24), 2261–2272. doi:10.1016/j.compstruc.2011.08.009

González, A., Casero, M., & Feng, K. (2020). Sensitivity to damage of the forced frequencies of a simply supported beam subjected to a moving quarter-car. Paper presented at the Proceedings of the 13th International Conference on Damage Assessment of Structures.

Gonzalez, A., OBrien, E. J., Cantero, D., Li, Y. Y., Dowling, J., & Znidaric, A. (2010). Critical speed for the dynamics of truck events on bridges with a smooth road surface. *Journal of Sound and Vibration, 329*(11), 2127–2146. doi:10.1016/j.jsv.2010.01.002

Gonzalez, A., Rattigan, P., OBrien, E. J., & Caprani, C. (2008). Determination of bridge lifetime dynamic amplification factor using finite element analysis of critical loading scenarios. *Engineering Structures, 30*(9), 2330–2337. doi:10.1016/j.engstruct.2008.01.017

Gonzalez, A., Rowley, C., & OBrien, E. J. (2008). A general solution to the identification of moving vehicle forces on a bridge. *International Journal for Numerical Methods in Engineering, 75*(3), 335–354. doi:10.1002/nme.2262

Green, M. F., & Cebon, D. (1997). Dynamic interaction between heavy vehicles and highway bridges. *Computers & Structures, 62*(2), 253–264. doi:10.1016/S0045-7949(96)00198-8

Kim, C.-Y., Jung, D.-S., Kim, N.-S., Kwon, S.-D., & Feng, M. Q. (2003). Effect of vehicle weight on natural frequencies of bridges measured from traffic-induced vibration. *Earthquake Engineering and Engineering Vibration, 2*(1), 109–115. doi:10.1007/BF02857543

Li, J. Z., Su, M. B., & Fan, L. C. (2003). Natural frequency of railway girder bridges under vehicle loads. *Journal of Bridge Engineering, 8*(4), 199–203. doi:10.1061/(ASCE)1084-0702(2003)8:4(199)

Li, J. T., Zhu, X. Q., Law, S. S., & Samali, B. (2020). Time-varying characteristics of bridges under the passage of vehicles using synchroextracting transform. *Mechanical Systems and Signal Processing, 140*, 106727. doi:10.1016/j.ymssp.2020.106727

Matsuoka, K., Kaito, K., & Sogabe, M. (2020). Bayesian time–frequency analysis of the vehicle–bridge dynamic interaction effect on simple-supported resonant railway bridges. *Mechanical Systems and Signal Processing, 135*, 106373. doi:10.1016/j.ymssp.2019.106373

Michaltsos, G. T., & Raftoyiannis, I. G. (2012). *Bridges' dynamics*. Oak Park, IL: Bentham eBooks.

Milana, G., Banisoleiman, K., & González, A. (2021). An investigation into the moving load problem for the lifting boom of a ship unloader. *Engineering Structures, 234*, 111899. doi:10.1016/j.engstruct.2021.111899

Mohammed, O., & González, A. (2017). Static and dynamic moments for any plane within a straight solid slab bridge caused by the crossing of a truck. *Engineering Structures, 150*, 465–480. doi:10.1016/j.engstruct.2017.07.059

OBrien, E. J., Cantero, D., Enright, B., & Gonzalez, A. (2010). Characteristic dynamic increment for extreme traffic loading events on short and medium span highway bridges. *Engineering Structures, 32*(12), 3827–3835. doi:10.1016/j.engstruct.2010.08.018

OBrien, E. J., Rattigan, P., Gonzalez, A., Dowling, J., & Znidaric, A. (2009). Characteristic dynamic traffic load effects in bridges. *Engineering Structures, 31*(7), 1607–1612. doi:10.1016/j.engstruct.2009.02.013

OECD. (1998). *Dynamic interaction between vehicles and infrastructure experiment (DIVINE)*. Final report. Paris, France.

Pinkaew, T., & Asnachinda, P. (2007). Experimental study on the identification of dynamic axle loads of moving vehicles from the bending moments of bridges. *Engineering Structures, 29*(9), 2282–2293. doi:10.1016/j.engstruct.2006.11.017

Rowley, C. W., OBrien, E. J., Gonzalez, A., & Znidaric, A. (2009). Experimental testing of a moving force identification bridge weigh-in-motion algorithm. *Experimental Mechanics, 49*(5), 743–746. doi:10.1007/s11340-008-9188-3

Sobol, I. M. (2001). Global sensitivity indices for nonlinear mathematical models and their Monte Carlo estimates. *Mathematics and Computers in Simulation, 55*(1–3), 271–280. doi:10.1016/s0378-4754(00)00270-6

Tedesco, J. W., McDougal, W. G., & Ross, C. A. (1999). *Structural dynamics: Theory and applications*. Menlo Park, CA: Addison Wesley Longman.

Weaver, W., & Johnston, P. R. (1987). *Structural dynamics by finite elements*. London: Prentice-Hall.

Yang, Y. B., Cheng, M. C., & Chang, K. C. (2013). Frequency variation in vehicle-bridge interaction systems. *International Journal of Structural Stability and Dynamics, 13*(2), 1350019. doi:10.1142/S0219455413500193

Yang, Y. B., Yao, Z., & Wu, Y. S. (2004). *Vehicle-bridge interaction dynamics: With applications to high-speed railways*. River Edge, NJ: World Scientific.

Yu, L., & Chan, T. H. T. (2007). Recent research on identification of moving loads on bridges. *Journal of Sound and Vibration, 305*(1–2), 3–21. doi:10.1016/j.jsv.2007.03.057

Zhai, W., Han, Z., Chen, Z., Ling, L., & Zhu, S. (2019). Train–track–bridge dynamic interaction: A state-of-the-art review. *Vehicle System Dynamics, 57*(7), 984–1027. doi:10.1080/00423114.2019.1605085

Zhai, W., Xia, H., Cai, C., Gao, M., Li, X., Guo, X., … Wang, K. (2013). High-speed train–track–bridge dynamic interactions – Part I: Theoretical model and numerical simulation. *International Journal of Rail Transportation, 1*(1–2), 3–24. doi:10.1080/23248378.2013.791498

Zhu, X. Q., & Law, S. S. (2002). Dynamic load on continuous multi-lane bridge deck from moving vehicles. *Journal of Sound and Vibration, 251*(4), 697–716. doi:10.1006/jsvi.2001.3996

Zhu, X. Q., & Law, S. S. (2015). Structural health monitoring based on vehicle-bridge interaction: Accomplishments and challenges. *Advances in Structural Engineering, 18*(12), 1999–2015. doi:10.1260/1369-4332.18.12.1999